micromachines

MDPI

Review

Unlocking the Potential of $Ti_3C_2T_x$ MXene: Present Trends and Future Developments of Gas Sensing

Aviraj M. Teli [1,†], Sagar M. Mane [2,†], Rajneesh Kumar Mishra [3,*], Wookhee Jeon [4] and Jae Cheol Shin [1,*]

[1] Division of Electronics and Electrical Engineering, Dongguk University-Seoul, Seoul 04620, Republic of Korea; avteli.teli@gmail.com
[2] Department of Fiber System Engineering, Yeungnam University, 280 Dehak-Ro, Gyeongsan 38541, Gyeongbuk, Republic of Korea; manesagar99@gmail.com
[3] Department of Physics, Yeungnam University, Gyeongsan 38541, Gyeongbuk, Republic of Korea
[4] Department of Semiconductor, Convergence Engineering, Sungkyunkwan University, Suwon 16419, Gyeonggi, Republic of Korea; wookie92@skku.edu
* Correspondence: rajneeshmishra08@gmail.com (R.K.M.); jcshin@dgu.ac.kr (J.C.S.)
† These authors contributed equally to this work.

Abstract: In recent years, the need for future developments in sensor technology has arisen out of the changing landscape, such as pollution monitoring, industrial safety, and healthcare. MXenes, a 2D class of transition metal carbides, nitrides, and carbonitrides, have emerged as a particularly promising group in part due to their exceptionally high conductivity, large area, and tunable surface chemistry. Proposed future research directions, including material modification and novel sensor designs, are presented to maximize $Ti_3C_2T_x$ MXene-based sensors for various gas sensing applications. While recent progress in $Ti_3C_2T_x$ MXene-based gas sensors is reviewed, we consolidate their material properties, fabrication strategy, and sensing mechanisms. Further, the significant progress on the synthesis and applications of $Ti_3C_2T_x$ MXene-based gas sensors, as well as the innovative technologies developed, will be discussed in detail. Interestingly, the high sensitivity, selectivity, and quick response times identified in recent studies are discussed, with specificity and composite formation highlighted to have a significant influence on sensor performance. In addition, this review highlights the limitations witnessed in real-life implementability, including stability, the possibility of achieving reproducible results, and interaction with currently available technologies. Prospects for further work are considered, emphasizing increased production scale, new techniques for synthesis, and new application areas for $Ti_3C_2T_x$ MXenes, including electronic nose and environmental sensing. Contemplating the existing works, further directions and the development framework for $Ti_3C_2T_x$ MXene-based gas sensors are discussed.

Keywords: $Ti_3C_2T_x$ MXenes; surface functionalization; properties; sensor technology; gas sensing; future prospects

check for updates

Academic Editor: Sudeep Sharma

Received: 11 January 2025
Revised: 25 January 2025
Accepted: 28 January 2025
Published: 29 January 2025

Citation: Teli, A.M.; Mane, S.M.; Mishra, R.K.; Jeon, W.; Shin, J.C. Unlocking the Potential of $Ti_3C_2T_x$ MXene: Present Trends and Future Developments of Gas Sensing. *Micromachines* **2025**, *16*, 159. https://doi.org/10.3390/mi16020159

Copyright: © 2025 by the authors. Licensee MDPI, Basel, Switzerland. This article is an open access article distributed under the terms and conditions of the Creative Commons Attribution (CC BY) license (https://creativecommons.org/licenses/by/4.0/).

1. Introduction

Recently, there has been a great deal of interest in the development of advanced and versatile gas sensors as they are important for environmental monitoring, industrial safety, and healthcare. Volatile organic compounds (VOCs) are a major source of air pollution, and of concern for human health and the environment [1]. Air quality and plans for local pollution control means are dependent on monitoring the VOC level. Commonly used industry applications of VOCs are chemical production, painting, and surface coating [2]. These sectors are monitored to ensure compliance with workplace safety and regulatory

spaces to ensure that these sectors are thriving. A representative VOC, acetone, has medical and industrial uses [3]. The medical association of elevated acetone levels in human exhalation has already been documented, and the condition is used as a diagnostic and management tool [4]. Industrially, acetone is used as a solvent, so its presence in the workplace must be monitored to avoid exposure hazards and promote workplace safety [5]. In addition, agricultural and industrial wastewater are polluted by ammonia [6]. Monitoring ammonia is vital to guard against water contamination and to determine the adequacy of water treatment processes [7]. Ammonia is also widely used in refrigeration systems and the fertilizer industry [8]. The risk to workers' health when releasing ammonia is critical to occupational safety and must be monitored [9]. On the other hand, industrial processes, including vehicle exhaust, are the source of most of the NO_2 emitted [10]. Also, levels of NO_2 are used for air quality monitoring and the control of pollution [11]. In addition, NO_2 concentration measurements are also essential to safeguard public health and serve as input into regulatory policy to reduce air pollution [12]. Excessive exposure to NO_2 is associated with chronic respiratory problems and the worsening of asthma [13]. The ability of advanced gas sensors to address the monitoring needs of these gases is critically vital for protecting human health, achieving industrial safety, and mitigating environmental impacts.

Two-dimensional (2D) materials, particularly MXenes, show great promise due to their exceptional structural, electrical, and chemical properties and offerings among the emerging solutions [14]. The general formula for MXenes, which represents the selective etching of precursor MAX phases, has been defined as $M_{n+1}X_nT_x$, where M stands for a transition metal, such as titanium (Ti), scandium (Sc), niobium (Nb), molybdenum (Mo), tantalum (Ta), or vanadium (V), which contributes to metallic conductivity and machinability; X denotes carbon or nitrogen, forming strong covalent bonds with the transition metal to impart hardness and resistance to oxidation and corrosion; and T_x pertains to the termination of the surface, such as -OH, -O, or -F [15–19]. Specifically, $Ti_3C_2T_x$ MXene, a member of the MXene family derived from layered transition metal carbides or nitrides, has demonstrated exceptional potential for gas sensing applications [20]. $Ti_3C_2T_x$ MXenes exhibit remarkable electronic properties attributed to their two-dimensional (2D) structure, comprising transition metal carbide layers interleaved with functional groups such as hydroxyl and fluorine terminations [21]. Moreover, the synthesis of $Ti_3C_2T_x$ MXene is a rapidly evolving field with several methods available, each offering unique advantages and challenges. The most common method for synthesizing $Ti_3C_2T_x$ MXene is through hydrofluoric acid (HF) etching [22,23]. In this approach, the MAX phase is immersed in concentrated HF, which selectively reacts with aluminum, forming AlF_3 and liberating hydrogen gas. The resultant $Ti_3C_2T_x$ MXene contains functional groups such as -F, -OH, and -O, enhancing its hydrophilicity. While this method is effective and straightforward, the use of highly toxic HF poses significant safety concerns, necessitating careful handling and disposal. Therefore, to address the hazards of HF, an alternative method involves in situ HF generation by reacting fluoride salts, such as LiF or NaF, with hydrochloric acid (HCl) [24,25]. This generates HF in a controlled manner, which then etches the Al layer from the MAX phase. On the other hand, $Ti_3C_2T_x$ MXene is also synthesized using alkali treatment, which employs strong bases like sodium hydroxide (NaOH) to etch the MAX phase [26]. This fluoride-free approach reduces environmental and safety concerns, but it is less effective and commonly used than acid-based methods. A recent innovation is molten salt etching, where the MAX phase is treated with molten salts, such as $ZnCl_2$ or LiCl-KCl, at high temperatures (550–700 °C) [27]. This method not only removes the aluminum layer but also allows for the tuning of the surface chemistry of the resulting MXenes. However, it requires specialized equipment and a higher energy input. These methods will enable

the production of high-quality MXenes tailored for various applications. The structure of $Ti_3C_2T_x$ MXene enables high electronic conductivity and offers plentiful active sites for gas molecule adsorption, thereby improving gas sensing performance [28]. Moreover, the surface chemistry of $Ti_3C_2T_x$ MXene can be tailored through selective functionalization or compositional modifications, offering versatility in the tuning of sensor selectivity and sensitivity towards specific gases [29]. $Ti_3C_2T_x$ MXene-based gas sensors have witnessed significant advancements in recent years, marked by efforts to enhance sensor performance metrics, including response time, selectivity, and detection limits [30]. These efforts are complemented by computational studies and theoretical models that provide insights into the underlying gas sensing mechanisms at the atomic and molecular levels. Furthermore, integration strategies with novel nanomaterials, advanced fabrication techniques, and innovative sensor configurations have further propelled the development of $Ti_3C_2T_x$ MXene-based gas sensors toward practical applications [31–33]. Gas sensors are indispensable for industrial safety, environmental monitoring, and healthcare diagnostics. Despite wide use, conventional metal oxide-based gas sensors are limited to high operating temperatures and insufficient sensitivity at low concentrations. Interestingly, room-temperature gas sensing applications of MXenes, with their metallic conductivity, tunable surface chemistry, and hydrophilicity, are proposed to be a breakthrough for the material.

This review aims to provide a comprehensive understanding of the structure, morphology, and recent developments in the gas sensing applications of $Ti_3C_2T_x$ MXene. It discusses the fundamental electronic and optical properties of $Ti_3C_2T_x$ MXene that contribute to its effectiveness as a gas sensor, highlights vital achievements, and outlines current challenges and future directions for harnessing its full potential in gas sensing applications. In addition, this review provides a roadmap for researchers and engineers seeking to exploit $Ti_3C_2T_x$ MXene-based gas sensors for diverse and demanding environmental and industrial monitoring scenarios by synthesizing and analyzing the latest research findings. Finally, the review offers a summary and a discussion on outlooks for future progress.

2. Structural, Morphological, and Elemental Analyses

X-ray diffraction (XRD) is a versatile method for determining the crystallographic nature of $Ti_3C_2T_x$ MXene. $Ti_3C_2T_x$ MXene usually exhibits a layered structure with characteristics resembling graphene oxide, which forms layers of transition metal atoms in between layers of carbon atoms [34]. Depending on the stacked layer thickness, the lattice plane (002) may be detected at 0.9–1.0 nm, which represents the interlayer distance of different $Ti_3C_2T_x$ MXene layers [35]. Moreover, the reduced interlayer d-spacing in the range of 0.28 nm can be shown for the lattice plane (004), which exists at a smaller scattering angle compared to the (002) lattice plane of $Ti_3C_2T_x$ MXene [36]. Yao et al. discussed the XRD spectra of Ti_3AlC_2 and $Ti_3C_2T_x$ MXenes, as elucidated in Figure 1a [37]. It was observed that $Ti_3C_2T_x$ MXene showed various lattice planes, such as (002), (004), and (008). Based on Raman analysis, the Raman spectrum of $Ti_3C_2T_x$ exhibits peaks associated with a material structure, including disorder (D band), in-plane vibrations (G band), out-of-plane vibrations (M band), and signals from surface functional groups [38]. Such analysis provides valuable information on critical aspects such as the quality of the produced $Ti_3C_2T_x$ MXenes, the defects present, and the surface chemistry [39]. The Raman D band of $Ti_3C_2T_x$ concerns the vibrational modes related to disorder or defects in the MXene structure and is usually observed at an 800–1000 cm^{-1} wave number [40]. The Raman D band of $Ti_3C_2T_x$ MXene is reactive to defects, including vacancies, surface-terminating groups like -OH or -F, or a distorted lattice [41]. The Raman G band of $Ti_3C_2T_x$ MXene is usually observed at 1500–1600 cm^{-1} in the Raman spectrum [42]. In addition, the Raman

G band is connected with the E_{2g} phonon mode of $Ti_3C_2T_x$ MXene's structure [43]. This mode also entails oscillations of the carbon atoms in the Ti_3C_2 plane. It was reported that the intensity and position of the Raman G band can provide information about the structure and bonding of $Ti_3C_2T_x$ MXene. It was also observed that the Raman M band is related to the out-of-plane vibrations of the Ti atoms in the $Ti_3C_2T_x$ structure [44]. Typically found in the range of 300 to 400 cm^{-1}, the intensity of its signal can depend on stacking and interlayer interactions between the $Ti_3C_2T_x$ MXene sheets [45]. Besides the known strong D, G, and M Raman bands, $Ti_3C_2T_x$ Raman spectra can also feature additional bands associated with the specific vibrational modes of functional groups covalently attached to the $Ti_3C_2T_x$ MXene surface (T_x groups) [46]. Iqbal et al. discussed the Raman spectra of Ti_3AlC_2 and $Ti_3C_2T_x$ MXenes, as depicted in Figure 1b [47]. The vibrational Raman peaks ω_1, ω_2, ω_3, and ω_4 are characteristic of the shear and longitudinal oscillations of Ti and Al atoms, which are observed in the spectra of the MAX phase at approximately 269 cm^{-1}, 423 cm^{-1}, and 613 cm^{-1}. Furthermore, the ω_1 peak due to Al vibrations disappears in the Mxene spectrum, indicating the successful etching of Al atoms and incorporation into the Mxene structure. The Mxene spectrum exhibits a prominent peak at about 151 cm^{-1} that suggests this Ti_3C_2 is oxidized, presumably as a result of increased surface reactivity. Additionally, a peak at 208 cm^{-1}, due to out-of-plane vibrations in the Ti and C, indicates the incorporation of functional groups such as -OH and -F during the etching process.

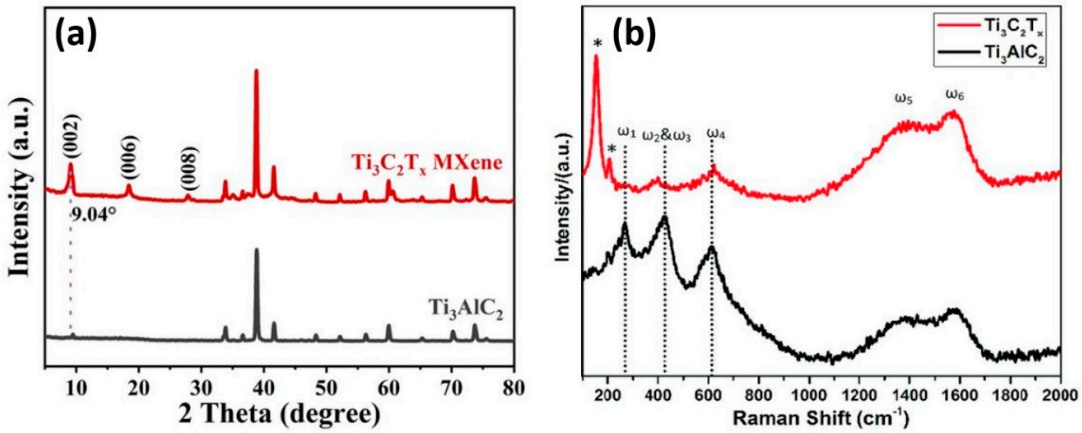


Figure 1. (**a**) XRD patterns of Ti_3AlC_2 and $Ti_3C_2T_x$ MXenes. Reproduced with permission from Ref. [37]. Copyright (2021) Springer Nature. (**b**) Raman spectra of Ti_3AlC_2 and $Ti_3C_2T_x$ MXenes (* represents out of plane vibrations of Ti and C). Reproduced with permission from Ref. [47]. Copyright (2021) MDPI.

The nature of the functional groups, such as -OH and -F, and their interaction with the Ti_3C_2 lattice leads to the appearance of these Raman bands at different frequencies [48]. Interestingly, XPS is a valuable tool for characterizing the elemental composition, chemical bonding states, and surface chemistry of $Ti_3C_2T_x$. The Ti 2p core level in XPS of $Ti_3C_2T_x$ is found at about 458–460 eV for Ti^{2+} and 454–456 eV for Ti^{3+} [49]. Additionally, the Ti^{2+} peak indicates titanium in a reduced state, generally related to Ti-C bonding [50]. Also, the Ti^{3+} peak represents the higher binding-energy states of the titanium in its oxidized form, commonly linked with Ti-O or Ti-F bonding [51]. The binding energies may depend slightly on surface termination (T_x) factors. The C 1s peak is typically observed at 281–284 eV with the ability to deconvolute to C-C/C-Ti, C-OH, and C=O [52] in the Ti_3C_2 carbon layers, or directly bound to titanium. The surface binds with the hydroxyl groups (C-OH) of carbon atoms on the surface. Oxygen on the MXene surface is indicated by the presence of carbonyl (C=O) groups [53]. This surface chemistry and functionalization of $Ti_3C_2T_x$ is revealed in the relative intensities and positions of these peaks. Interestingly, the O

1s peaks appear at 530–532 eV, and F 1s peaks at 685–688 eV [54]. In addition, the XPS can distinguish further surface functional groups from hydroxyl (-OH), oxide (-O), and fluoride (-F) terminations. Understanding the surface reactivity, electronic properties, and interactions of the $Ti_3C_2T_x$ is dependent upon the presence and relative abundance of these groups. Wang et al. reported the plasma-oxidized $Ti_3C_2T_x$ MXene and its XPS spectra to discuss its chemical composition, as shown in Figure 2a–f [55]. Figure 2a shows the changes induced at the atomic level, which are presented by the schematic representation of the $Ti_3C_2T_x$ MXene structure before and after oxygen plasma treatment. The MXene structure before plasma treatment consists of layers of titanium carbide (Ti_3C_2) with surface terminations -OH, -F, and -O, which result from the etching process in the synthesis. It is made clear that these surface terminations are essential to $Ti_3C_2T_x$ MXene's electrical, chemical, and mechanical properties. In the oxygen plasma-treated $Ti_3C_2T_x$ MXene, the existing terminations are removed or altered, and oxygen functionalities are introduced.

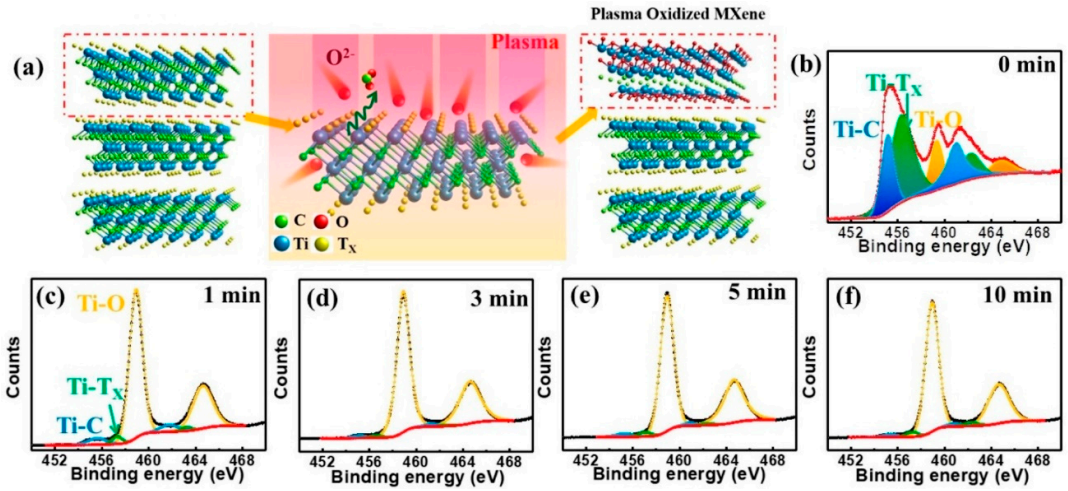


Figure 2. (**a**) A schematic illustration of the $Ti_3C_2T_x$ MXene structure before and after oxygen plasma treatment, and (**b**–**f**) the Ti 2p core-level XPS spectra of the MXene exposed to oxygen plasma for 0, 1, 3, 5, and 10 min, respectively. Reproduced with permission from Ref. [55]. Copyright (2021) American Chemical Society.

Figure 2b illustrates the XPS spectra of the Ti 2p core-level XPS spectra, used for a detailed study of the oxygen plasma-treated surface chemistry. Figure 2b shows that the XPS spectrum of $Ti_3C_2T_x$ MXene recorded at 0 min features prominent peaks due to Ti-T_x, Ti-C, and Ti-O bonds. On the other hand, the XPS spectra in Figure 2c–f display progressive shifts and changes in the Ti_{2p} peak intensity with increasing plasma exposure time (1, 3, 5, and 10 min). These transformations correspond to the switching of surface terminations from oxygen-deficient to oxygen-rich groups. Therefore, these unique structural and elemental characterization techniques are pivotal in determining the structural, electronic, surface termination, and chemical properties of $Ti_3C_2T_x$ MXene. These features make $Ti_3C_2T_x$ MXenes highly suitable for applications in gas sensing, where sensitivity, selectivity, and stability are critical requirements. In addition, titanium (Ti) contributes to the high electrical conductivity of $Ti_3C_2T_x$ MXenes, facilitating the fast charge transport that is essential for improved gas sensing applications. Additionally, Ti forms strong covalent bonds with carbon, ensuring structural stability under various conditions, which is also vital for the gas sensor's stability. The d-orbital electrons of Ti also enhance gas detection, enabling stronger interactions with gas molecules, which is vital for achieving high sensitivity in gas sensors. The carbon layers within the $Ti_3C_2T_x$ MXene structure provide a conductive backbone and mechanical flexibility, which are advantageous for flexible and wearable gas sensing devices. Surface terminations (-T_x), such as -O, -OH, and -F, introduced during

the synthesis process significantly influence the chemical reactivity, hydrophilicity, and surface energy of $Ti_3C_2T_x$ MXene. These functional groups enhance the adsorption of polar gas molecules, such as NH_3 or NO_2, by creating active sites for interaction. The layered structure of $Ti_3C_2T_x$ MXenes, with tunable interlayer spacing, further supports gas diffusion and adsorption, improving their selectivity for specific gases. This ability to tailor the surface chemistry and structure is a key advantage of MXenes over other materials used for gas sensing.

Hu et al. reported on hierarchical $Ti_3C_2T_x$ MXene/carbon nanotubes as illustrated in Figure 3a–f [56]. Figure 3a–g elucidate the schematic synthesis process, morphology, structure, and elemental characteristics of the hierarchical $Ti_3C_2T_x$ MXene/carbon nanotubes, reflecting its architecture and composition. In the schematic [Figure 3a], the $Ti_3C_2T_x$ MXene/carbon nanotubes are prepared, deposited onto composite nanofibers, and processed to form a tubular structure via electrospinning. By using self-sacrificial templating, the formation of the rigid, aligned tubular architecture of $Ti_3C_2T_x$ MXene/carbon nanotubes is facilitated. Figure 3b–d reveal that the morphology of the $Ti_3C_2T_x$ MXene/carbon nanotubes is highly organized, consisting of a tubular form as determined by SEM. In addition, the calcined nanotubes have an average diameter of approximately 1.5 μm, exhibiting a wrinkled surface. An optimal MXene to polymer ratio during synthesis was found to preserve the tubular morphology. Further insights into the exact structure of the $Ti_3C_2T_x$ MXene/carbon nanotubes are provided by high-resolution transmission electron microscopy (HRTEM) images, as shown in Figure 3e,f, which show the ultrathin MXene layers of the $Ti_3C_2T_x$ MXene/carbon nanotubes. The layered structure turns out to be ductile and folded, with interlayer spacings expanded to approximately 0.95 nm. In addition, the inner surface of the nanotubes is covered by a thin layer of carbon obtained by the pyrolysis of the polymer template, which contributes to the stability of the structure. Figure 3g shows the elemental mapping of the $Ti_3C_2T_x$ MXene/carbon nanotubes and confirms the uniform C, O, and Ti distribution throughout the $Ti_3C_2T_x$ MXene/carbon nanotube heterostructure. The successful integration of $Ti_3C_2T_x$ MXene with carbon nanotubes, confirmed by this even dispersion, also supports the stability of their structure. In addition, Wang et al. discussed SEM imagery of MXene–Ti_3C_2, which features a layered structure, as depicted in Figure 3h [57]. The high-magnification SEM image in Figure 3h highlights the distinct multilayer structure of the MXene–Ti_3C_2, with an average layer thickness of less than 20 nm. This well-exfoliated 2D layered structure plays a critical role in enhancing the gas sensing properties of the MXene–Ti_3C_2. The multilayered configuration of MXene–Ti_3C_2 provides a significantly high surface area, allowing a greater density of adsorption sites for gas molecules. This increased surface area improves the sensitivity of the MXene–Ti_3C_2 by enabling more interactions with target gases. Wang et al. reported on SEM imagery of $Ti_3C_2T_x$ MXene, as portrayed in Figure 3i, revealing its characteristic accordion-like morphology with significant interlayer spacing [58]. This unique morphology is highly advantageous for gas sensing applications due to several key factors, such as the accordion-like structure providing a substantially increased surface area, ensuring more active sites on the surface of the $Ti_3C_2T_x$ MXene, which is critical for the adsorption and desorption of various gas molecules. Zhang et al. described SEM imagery of $Ti_3C_2T_x$ MXene, as exposed in Figure 3j, demonstrating the transformation of Ti_3AlC_2 MAX into $Ti_3C_2T_x$ MXene following the etching of the Al layer [59]. This process results in a 2D layered morphology, which significantly enhances the properties of the $Ti_3C_2T_x$ MXene, making it highly suitable for gas sensing applications. The removal of the Al layer creates expanded interlayer spacing and a high surface area, which is crucial for improving gas adsorption capacity. In addition, the metallic conductivity of $Ti_3C_2T_x$ MXene is another vital characteristic for gas sensing applications. $Ti_3C_2T_x$ MXenes are ideal for detecting

changes in electrical resistance or conductivity caused by gas adsorption. When target gas molecules interact with the surface of $Ti_3C_2T_x$ MXenes, the electrical changes are measurable, allowing for efficient gas detection, ensuring a rapid response to the presence of gas molecules, which is essential for real-time sensing applications. Moreover, modifying the surface functional groups of $Ti_3C_2T_x$ MXene, such as -OH, -F, or -O are essential to improve the selective detection for specific gas molecules, which are filled with various interfering gases. Such functionalization ensures that the $Ti_3C_2T_x$ MXene responds predominantly to the desired gas, reducing interference from other gases in the environment.

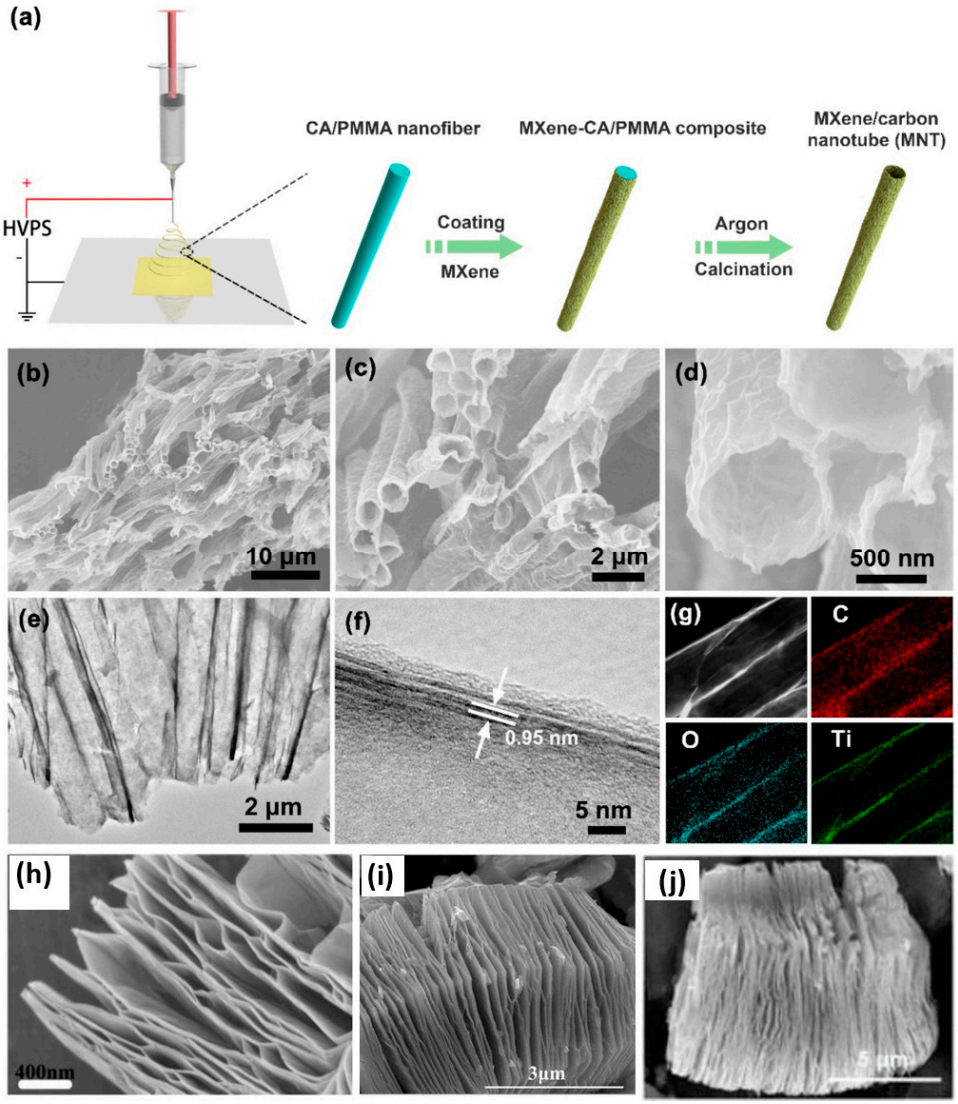


Figure 3. (**a**) A schematic illustration of the synthetic route for the $Ti_3C_2T_x$ MXene/carbon nanotube; (**b**–**d**) SEM images of the morphology of the $Ti_3C_2T_x$ MXene/carbon nanotube at various magnifications; (**e**,**f**) high-resolution transmission electron microscopy (HRTEM) images of the internal structure and lattice fringes of the $Ti_3C_2T_x$ MXene/carbon nanotube; and (**g**) elemental mapping of C, O, and Ti elements of the $Ti_3C_2T_x$ MXene/carbon nanotube showing the uniformity of the material composition. Reproduced with permission from Ref. [56]. Copyright (2021) American Chemical Society. (**h**) A high-magnification SEM image of MXene–Ti_3C_2. Reproduced with permission from Ref. [57]. Copyright (2015) Institute of Physics. (**i**) An SEM image of $Ti_3C_2T_x$ MXene. Reproduced with permission from Ref. [58]. Copyright (2020) Wiley-VCH GmbH. (**j**) An SEM image of $Ti_3C_2T_x$ MXene. Reproduced with permission from Ref. [59]. Copyright (2024) American Chemical Society.

3. Properties

3.1. Optical

$Ti_3C_2T_x$ MXene exhibits interesting optical properties due to its unique structure and composition. $Ti_3C_2T_x$ MXene is generally transparent in the visible to near-infrared spectrum, which makes it suitable for applications in transparent electrodes and optoelectronics [60]. This transparency is attributed to its layered structure, where the $Ti_3C_2T_x$ MXene layers allow light to pass through. Depending on their specific composition and structure, $Ti_3C_2T_x$ MXenes can exhibit plasmonic resonances in the infrared and terahertz frequencies [61]. These plasmonic properties are useful in sensing applications and for enhancing light–matter interactions. $Ti_3C_2T_x$ MXene shows absorption in the ultraviolet (UV) region, primarily due to transitions between the valence and conduction bands [62]. The absorption edge typically covers into the visible spectrum, influencing its optical properties [63]. $Ti_3C_2T_x$ MXene is reported to have a direct band gap, which means that the energy difference between the valence band and the conduction band occurs at the same momentum (k) point in the Brillouin zone [64]. Direct band gaps favor optoelectronic applications such as photodetectors and light-emitting devices. The band gap of $Ti_3C_2T_x$ MXene can be influenced by various factors, including surface functionalization, which alters the optical properties. By adjusting the surface terminations (T_x), researchers can tune the band gap of $Ti_3C_2T_x$ MXene for specific applications [65]. The experimental studies have reported band gaps in $Ti_3C_2T_x$ MXenes ranging from approximately 0.5 eV to 2.5 eV, depending on the specific synthesis method, degree of surface functionalization, and layer thickness [66]. Modulating the band gap makes $Ti_3C_2T_x$ MXene versatile for various applications, from energy storage to photovoltaics [67]. Furthermore, $Ti_3C_2T_x$ MXene exhibits transparency in the visible spectrum, plasmonic resonances in the infrared, and a tunable direct band gap that can be tailored through surface modifications [68]. These properties make $Ti_3C_2T_x$ MXene a promising material for next-generation optoelectronics, sensors, and other emerging technologies. Further, the photoluminescence (PL) peaks of $Ti_3C_2T_x$ MXene arise primarily from surface functional groups and defects [69]. These groups can introduce energy levels within the band gap of the $Ti_3C_2T_x$ MXene, leading to the emission of light when excited [70]. The PL emission spectrum of $Ti_3C_2T_x$ MXene typically depends on the excitation wavelength. This dependence suggests that different energy states or defects of the $Ti_3C_2T_x$ MXene contribute to this emission, each responding differently to excitation energy [71]. The emission spectrum of $Ti_3C_2T_x$ MXene ranges from visible to near-infrared wavelengths [72]. The emitted light can be tuned by modifying the surface chemistry through functionalization or controlling the synthesis conditions of the $Ti_3C_2T_x$ MXene [73]. The PL properties make $Ti_3C_2T_x$ MXene suitable for sensing applications, such as detecting gases, biomolecules, or environmental pollutants. $Ti_3C_2T_x$ MXene could potentially be integrated into optoelectronic devices, which emit light under certain conditions, opening possibilities for applications in LEDs, displays, and even as components in photonic circuits [74]. The near-infrared emissions of $Ti_3C_2T_x$ MXene are particularly advantageous for biomedical imaging due to their deeper tissue penetration and reduced autofluorescence from biological samples [75]. The FTIR spectra of $Ti_3C_2T_x$ MXene typically show characteristic peaks related to oxygen-containing functional groups (OH, C=O), carbonaceous species (C-H, C-C), Ti-C bonds, and interlayer water [76]. These peaks' exact positions and intensities provide information about the synthesis method, surface chemistry, and oxidation state of the $Ti_3C_2T_x$ MXene. The hydroxyl groups (OH) are typically observed around 3000–3700 cm^{-1} (broad peak) and around 1400–1600 cm^{-1} (shoulder peak) [77]. The presence of hydroxyl groups in the $Ti_3C_2T_x$ MXene indicates the presence of water or surface hydroxyls. On the other hand, the carbonyl groups (C=O) appear around 1700–1750 cm^{-1}, which indicates the presence of surface-adsorbed species

or oxidation states on the $Ti_3C_2T_x$ MXene. Further, oxide groups (Ti-O-Ti) in the $Ti_3C_2T_x$ MXene are observed around 400–800 cm^{-1} [78]. These bands indicate the presence of TiO_x species in the $Ti_3C_2T_x$ MXene, which can form due to oxidation during synthesis or exposure to air. In addition, the C-H stretching and bending of $Ti_3C_2T_x$ MXene can be observed around 2800–3000 cm^{-1} and 1300–1500 cm^{-1}, respectively [79]. Also, C-C and C=C bonds in $Ti_3C_2T_x$ MXene typically appear in the 1000–1500 cm^{-1} range [80]. The Ti-C bonds of $Ti_3C_2T_x$ MXene are a broad feature in the 600–800 cm^{-1} region [81]. The exact position can vary depending on the titanium's chemical environment and oxidation state. Additional peaks related to surface functional groups such as -F, -Cl, or -O may be observed depending on the synthesis method and subsequent processing [82].

Kumar et al. discussed the absorption spectrum and evaluated the optical band gap of $Ti_3C_2T_x$ MXene, as depicted in Figure 4a,b [83]. Figure 4a reveals the UV–visible absorption spectrum of $Ti_3C_2T_x$ MXene, which illustrates a sharp peak at 300 nm attributed to surface functional groups (OH, O, F) created through the etching of the Al from the Ti_3AlC_2 MAX phase. In addition, a broad absorption peak centered at 690 nm is evidence of longitudinal plasmon resonance, typical of layered $Ti_3C_2T_x$ MXene nanomaterials. Based on these features, it is clear that the material is highly absorbent of light over a wide spectral range. Moreover, Figure 4b discloses a band gap of approximately 1.67 eV for the $Ti_3C_2T_x$ MXene, determined using Tauc's plot, showing the semiconducting nature of $Ti_3C_2T_x$ MXene. Zhang et al. discussed the photoluminescence (PL) spectra for excitation wavelength-dependent emission without the surface modification and with the surface modification of the $Ti_3C_2T_x$ MXene, as portrayed in Figure 4c,d [84]. Figure 4c depicts the PL spectrum of the $Ti_3C_2T_x$ MXene without surface modification. It illustrates three strong emissions from the $Ti_3C_2T_x$ MXene at 503 nm (green) for 405 nm excitation, 597 nm (yellow) for 532 nm excitation, and 652 nm (red) for 632.8 nm excitation. Further, the redshift of the PL spectrum with increasing excitation wavelength indicates that the PL arises from defect states, with $Ti_3C_2T_x$ MXene being deficient of the band gap that would be required for such emissions, and is likely associated with interspersed TiO_2 clusters. On the other hand, Figure 4d portrays that the PL peaks of the surface-modified $Ti_3C_2T_x$ MXene are further redshifted to 530 nm (green), 701 nm (yellow), and 759 nm (red). In the modification, the density and diversity of the defect energy states may be increased, broadening the range of PL emissions and decreasing the PL energy by 0.1–0.3 eV. These results emphasize the importance of defect engineering for tuning the optical properties of $Ti_3C_2T_x$ MXene. Elumalai et al. discussed the UV–visible NIR spectra of $Ti_3C_2T_x$ MXene, as described in Figure 4e [85]. Broad plasmon peaks originating from surface plasmon resonances (SP) and interband transitions inherent to $Ti_3C_2T_x$ MXene's structure are observed. Interestingly, the absorption characteristics are unchanged across different solvents, depicted in the spectra and inset photographs of Figure 4e. On the other hand, the robustness of the optical behavior of $Ti_3C_2T_x$ MXene is due to functional groups from the MXene surface (-F, -OH, -O) that control its interaction with light. Captivatingly, it possesses the adaptability to enhance its application in biosensing, chemical detection, and optoelectronic devices through the ability to fine-tune these properties by changing the solvent. Du et al. discussed the FTIR spectra of $Ti_3C_2T_x$ MXene, as designated in Figure 4f [86]. Figure 4f unveils the Fourier Transform Infrared (FTIR) spectra showing the structural and chemical composition of $TiO_2/Ti_3C_2T_x$ and $Ti_3C_2T_x$ MXenes. A characteristic peak of the anatase TiO_2 phase appears, corresponding to well-known peaks within the range of 800–500 cm^{-1}. In particular, the peak at 570 cm^{-1} is attributed to the deformation vibration of the Ti-O bond. The FTIR spectra display chemical modifications due to the interactions between the TiO_2 nanoparticles and the $Ti_3C_2T_x$ substrate, leading to a robust hybrid structure.

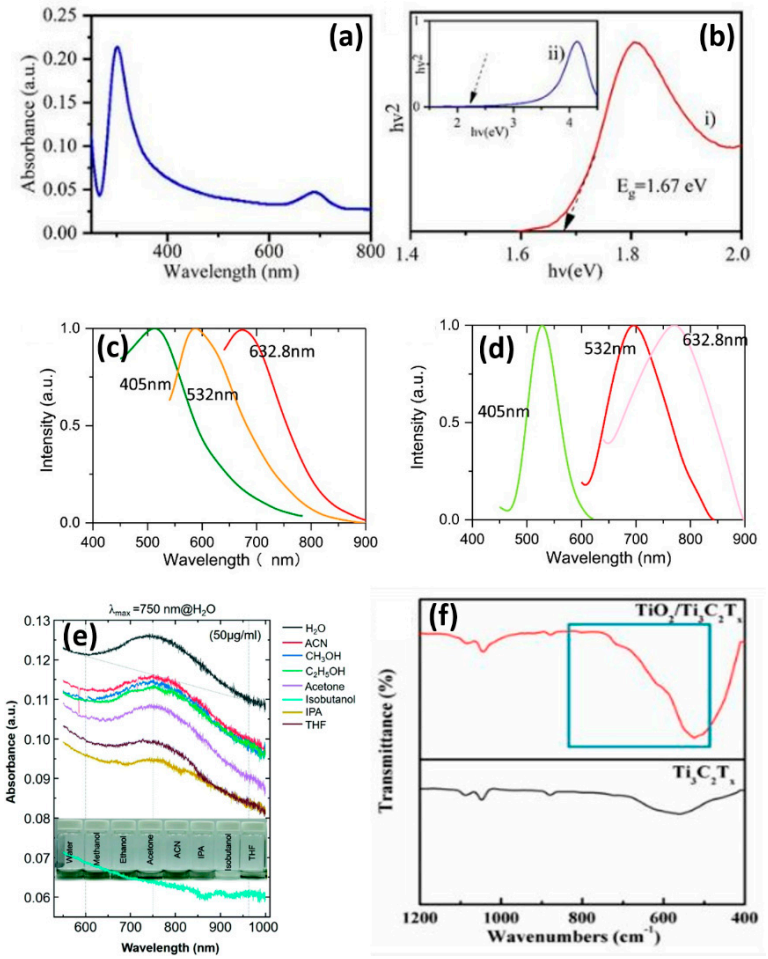


Figure 4. (**a**) UV–visible absorption spectrum and (**b**) related optical band gap of $Ti_3C_2T_x$ MXene. Reproduced with permission from Ref. [83]. Copyright (2024) Springer Nature. PL spectrum of $Ti_3C_2T_x$ MXene (**c**) without surface modification and (**d**) with surface modification at various excitation wavelengths. Reproduced with permission from Ref. [84]. Copyright (2019) Elsevier. (**e**) UV–visible NIR spectra of $Ti_3C_2T_x$ MXene and optical image in different solvents. Reproduced with permission from Ref. [85]. Copyright (2020) Royal Society of Chemistry. (**f**) FTIR spectra of $TiO_2/Ti_3C_2T_x$ and $Ti_3C_2T_x$ MXenes. Reproduced with permission from Ref. [86]. Copyright (2019) MDPI.

3.2. Magnetic

The titanium and carbon atoms present in $Ti_3C_2T_x$ MXene typically render paramagnetic behavior. In addition, the magnetic properties of $Ti_3C_2T_x$ MXene are very sensitive to surface terminations [87]. Typically surface functional groups govern the surface paramagnetic nature in $Ti_3C_2T_x$ MXene, which in turn affects the electronic structure and magnetic moment of Ti atoms [88]. Additionally, it has been observed that the magnetic behavior of $Ti_3C_2T_x$ MXene varies between different surface terminations [89]. Interestingly, the -OH terminations of $Ti_3C_2T_x$ MXene are expected to increase the magnetic moment compared with -F or -O terminations because of the electron donation from -OH groups to the Ti atoms resulting in enhanced spin density [90]. Furthermore, density functional theory (DFT) calculations have been carried out to predict the magnetic properties of $Ti_3C_2T_x$ MXenes [91]. Intriguingly, the magnetic properties of $Ti_3C_2T_x$ MXene are quite dependent on doping it with different materials [92]. It has been found that iron doping in $Ti_3C_2T_x$ can lead to strong ferromagnetic behavior [93]. The Fe atoms can also create localized magnetic moments due to their very nature, and facilitate interaction with the Ti atoms, to produce an increased overall magnetic moment on the $Ti_3C_2T_x$ MXene. Furthermore, the magnetic properties of $Ti_3C_2T_x$ MXene can also be improved by using cobalt (Co) and nickel (Ni)

doping [94]. These transition metals have unpaired d electrons, which can contribute to the magnetic moment and allow $Ti_3C_2T_x$ MXene to change from paramagnetic to ferromagnetic behavior [95]. Gadolinium (Gd) and neodymium (Nd) are also known rare earth elements, and their 4f electrons give them intense magnetic moments [96]. The magnetic properties of $Ti_3C_2T_x$ MXene can be significantly enhanced by doping with rare earth elements, and remarkably strong ferromagnetism can be achieved at room temperature [97]. Fascinatingly, $Ti_3C_2T_x$ MXene could support both the presence and absence of magnetism by virtue of boron doping [98]. Because boron atoms can produce local distortions on the lattice and change the spin distribution, they can increase the magnetic properties of $Ti_3C_2T_x$ MXene. Meanwhile, the doping of nitrogen in $Ti_3C_2T_x$ MXene has been demonstrated to enhance its magnetic behavior via interaction between the nitrogen atoms and titanium atoms in the $Ti_3C_2T_x$ MXene structure [99]. These hybrid/composite/heterostructures of $Ti_3C_2T_x$ MXene may also stimulate the modification of magnetic behavior. In addition, layered heterostructures of $Ti_3C_2T_x$ MXene with other two-dimensional materials, such as graphene or TMDs, can also impact its magnetic properties [100]. The magnetic behavior of the heterostructures can be altered through interlayer interactions and charge transfer between layers. Consequently, we conclude that $Ti_3C_2T_x$ MXene possesses interesting and tunable magnetic properties influenced primarily by surface terminations and doping with different materials [101].

Zhang et al. discussed the magnetic properties of $Ti_3C_2T_x$ (MX-as), $Ti_3C_2T_x$ at an annealing of temperature 100 °C (MX-100), $Ti_3C_2T_x$ at an annealing temperature of 300 °C (MX-300), and $Ti_3C_2T_x$ at an annealing temperature of 500 °C (MX-500), as depicted in Figure 5a–d [102]. Figure 5a reveals the magnetic properties of monolayer $Ti_3C_2T_x$ MXene samples before and after annealing in hydrogen (H_2) at different temperatures, presenting the magnetic susceptibilities (χ) of the MX-as, MX-100, MX-300, and MX-500 samples as a function of temperature (2–300 K) in a 1 kOe field. It is observed that the MX-as, MX-100, and MX-300 samples show a combination of Curie and Pauli paramagnetism. However, MX-500 deviated severely from this behavior, signaling the onset of magnetic ordering. At low temperatures $\chi^{-1}(T)$, MX-as, MX-100, and MX-300 could be well fitted by Curie's law, but MX-500 deviates from Curie's law, revealing ferromagnetic features appearing as temperature-dependent. Figure 5b divulges the magnified χ(T) curves of MX-as, MX-100, and MX-300 in the 180–300 K range, which show a dominance of Pauli paramagnetism. Figure 5c displays the magnetic moment (M) vs. the applied field (H) plot at 2 K under the applied field of 65 kOe. Successively, M_s increases progressively with annealing temperature, indicating substantial improvement in MX-500. Figure 5d shows the hysteresis loop of MX-500 at 2 K and 300 K. Ferromagnetic order was confirmed by the loop showing a clear coercive field (H_c) of ~84 Oe and remnant magnetization (M_r) ~0.002 emu/g at 2 K, which illustrates ferromagnetism. It is found that the magnetic properties are enhanced, including the emergence of ferromagnetism in MX-500, causing the formation of Ti-C vacancy pairs. Zhang et al. reported the enhanced microwave absorption properties of the $Ti_3C_2T_x$, as revealed in Figure 5e,f [103]. As shown in Figure 5e, the Fe_3O_4@$Ti_3C_2T_x$ composites exhibit ferromagnetic behavior with a clear magnetic hysteresis loop. It is found that the Fe_3O_4 content changes the values of key parameters, such as the saturation magnetization (M_s), remnant magnetization (M_r), and coercive field (H_c). In particular, as the concentration of Fe_3O_4 grows, the saturation magnetization increases from 11.19 emu/g up to 41.20 emu/g. Therefore, these magnetic behaviors are attributed to microwave absorption performance factors, such as increased magnetic loss and energy dissipation. Figure 5f exhibits the evolution of the specific surface area at different contents of Fe_3O_4 in the Fe_3O_4@$Ti_3C_2T_x$ composites. Interestingly, the presence of a 30 wt% of Fe_3O_4 in Fe_3O_4@$Ti_3C_2T_x$ significantly increases its specific surface area to maximum as compared

with $Ti_3C_2T_x$. Furthermore, enhanced interface polarization is possible due to the improved specific surface area. However, it also increases the dielectric loss mechanisms, which are highly critical to successful microwave absorption. On the other hand, it is observed that the synergetic role of Fe_3O_4 in Fe_3O_4@$Ti_3C_2T_x$ improves the magnetic and surface feature properties.

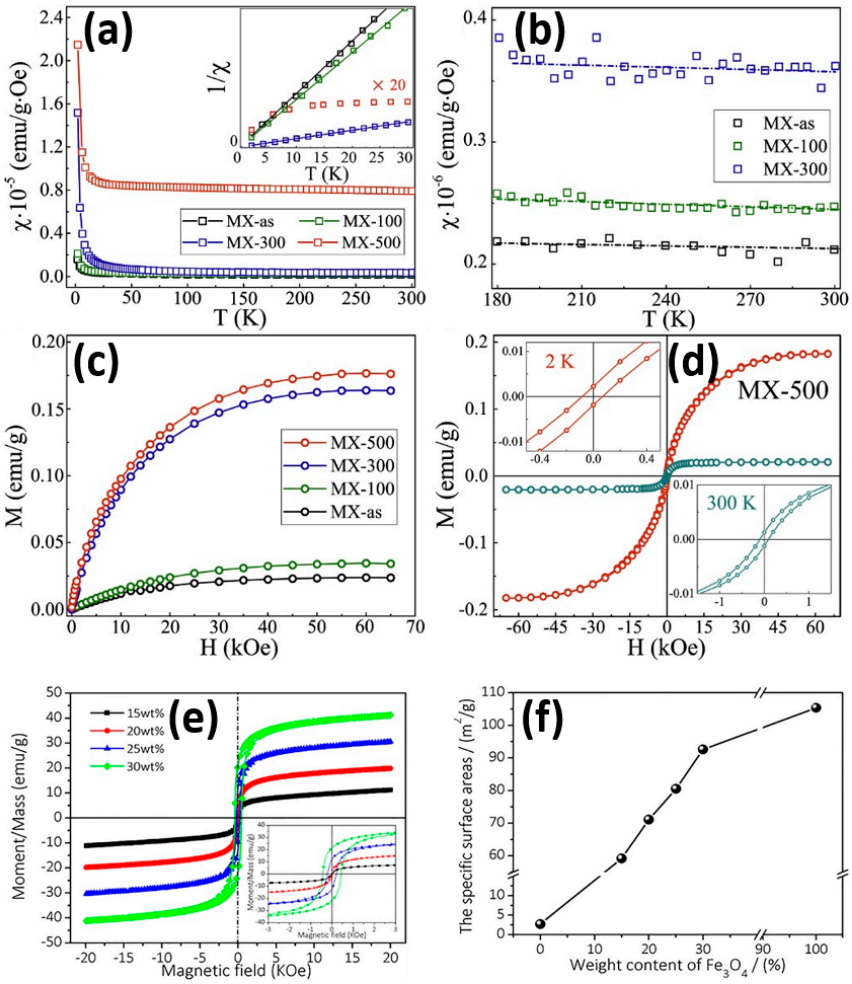


Figure 5. (**a**) Magnetic susceptibility, $\chi(T)$, curves measured from 2 to 3000 K under 1 kOe field; (**b**) closer examination of $\chi(T)$ curves for $Ti_3C_2T_x$ (MX-as), $Ti_3C_2T_x$ at annealing temperature 100 °C (MX-100), $Ti_3C_2T_x$ at annealing temperature 300 °C (MX-300), and $Ti_3C_2T_x$ at annealing temperature 500 °C (MX-500) in temperature range from 180 to 300 K; (**c**) magnetic moment (M) vs. applied field H plots at 2 K; and (**d**) hysteresis loop for MX-500 at 2 K and 300 K. Reproduced with permission from Ref. [102]. Copyright (2020) Elsevier. (**e**) Hysteresis loops of Fe_3O_4@$Ti_3C_2T_x$ with different concentration of Fe_3O_4, and (**f**) specific surface area of Fe_3O_4, $Ti_3C_2T_x$ MXene, and Fe_3O_4@$Ti_3C_2T_x$ vs. Fe_3O_4 concentration plot. Reproduced with permission from Ref. [103]. Copyright (2019) Elsevier.

3.3. Electronic

$Ti_3C_2T_x$ MXenes are most studied due to their fascinating electronic properties, where T stands for surface terminations, such as -OH, -O, and -F [53]. $Ti_3C_2T_x$ MXene exhibits metallic or semi-metallic behavior with high electrical conductivity [104]. This is attributed to the presence of conductive Ti-C bonds within its layers and the contribution of the d electrons from titanium. In addition, the electronic band structure of $Ti_3C_2T_x$ MXene can be tuned by modifying its surface terminations. Typically, $Ti_3C_2T_x$ MXene with -OH and -O terminations exhibits metallic behavior, while -F terminations can open a small band gap, potentially altering its semiconducting properties [105]. The mobility of charge carriers

in $Ti_3C_2T_x$ MXene is relatively high, making it suitable for electronic device applications. Also, the surface terminations of the $Ti_3C_2T_x$ MXene can influence the carrier concentration, density of states (DOS) near the Fermi level, and scattering mechanisms, influencing overall mobility [106]. Interestingly, it has been found that the presence of -O terminations tends to increase the DOS at the Fermi level, enhancing metallic properties; however, -F terminations can decrease the DOS at the Fermi level [107]. Also, it has been observed that the work function of $Ti_3C_2T_x$ MXene is dependent on its surface chemistry and found to be between 4 and 5 eV, which is suitable for various electronic and optoelectronic applications [108]. Moreover, metal (Au, Pd, Pt, and Ag) doping can increase its inclusive electrical conductivity by introducing additional free electrons or holes in the $Ti_3C_2T_x$ MXene [109]. In addition, doping with noble metals can also modify the work function, which makes $Ti_3C_2T_x$ MXene more suitable for specific applications, such as catalysts or sensors [110]. Furthermore, non-metal dopants such as nitrogen, boron, and phosphorous can introduce states in the band gap or shift the conduction/valence bands, which effectively modulates the band gap of $Ti_3C_2T_x$ MXene [111]. Excitingly, nitrogen doping is extremely important, as it changes metallic $Ti_3C_2T_x$ MXene into semiconductor $Ti_3C_2T_x$ MXene. It has also been studied that transition metals such as iron, cobalt, and nickel doping can introduce magnetic moments in $Ti_3C_2T_x$ MXene, which makes it a more suitable candidate for spintronic applications [112]. Therefore, it is concluded that $Ti_3C_2T_x$ MXene is a versatile material with tunable electronic properties, making it ideal for a wide range of applications. Further, doping with different materials allows for precise control over its electronic structure, conductivity, work function, and other vital properties, opening up new possibilities in various applications.

Anasori et al. reported the electronic properties of MXenes by modulating their transition metal layers, as exposed in Figure 6a–c [113]. Figure 6a illustrates the resistivity behavior of $Ti_3C_2T_x$ MXene and Mo-containing MXenes ($Mo_2TiC_2T_x$ and $Mo_2Ti_2C_3T_x$) as a function of temperature. $Ti_3C_2T_x$ MXene presents metallic behavior with decreasing resistivity between 250 K and 130 K. On the other hand, $Mo_2TiC_2T_x$ and $Mo_2Ti_2C_3T_x$ exhibit semiconductor-like behaviors, of which the resistivity increases with decreasing temperatures between 250 K and 130 K. Interestingly, it was found that replacing the outer titanium layers with molybdenum basically changed the electronic properties. Figure 6b demonstrates the resistivity differences between multilayered $Mo_2TiC_2T_x$ and $Ti_3C_2T_x$ MXenes. It shows the metallic behavior down to ~130 K of $Ti_3C_2T_x$ MXene before an upsurge in its resistivity at lower temperatures. On the other hand, the resistivity of $Mo_2TiC_2T_x$ increases monotonically with decreasing temperature and illustrates semiconducting behavior. Fascinatingly, it was concluded that the transition from metallic to semiconductor-like properties was due to molybdenum substitution. Figure 6c elucidates the differences in transport mechanisms in magnetoresistance measurements at 10 K. Negative MR is also found for the $Ti_3C_2T_x$ MXene, ascribed to weak localization effects due to negative magnetoresistance. In contrast, the magnetoresistance shows positive behavior in the $Mo_2TiC_2T_x$. Moreover, the magnetoresistance behaviors of $Ti_3C_2T_x$ and $Mo_2TiC_2T_x$ MXenes diverge from each other, suggesting fundamentally different electron transport mechanisms, solidifying molybdenum as a strong contributor to the electronic structure. Chu et al. described the electronic properties of $Ti_3C_2T_x$ MXene by a first-principles study, as revealed in Figure 6d–f [114]. Figure 6d depicts the electronic band structure and bonding properties of multilayer $Ti_3C_2T_x$ MXene. The electronic band structure and density of the states calculated from the multilayer MXene confirm metallic characteristics, as shown in Figure 6d,e. It is observed that the relation of surface terminations to the electronic properties of the multilayer $Ti_3C_2T_x$ MXene structure is demonstrated by the presence of finite electronic states near the metal junction Fermi level, predominantly due to terminating groups H, F, and O. Figure 6f reveals a Crystal Orbital Hamilton Population

(COHP) analysis of the bonding characteristics between adjacent layers. For H-O and H-F atomic pairs, the COHP analysis illustrates bonding features close to the Fermi level and finds the formation of H-bonds between adjacent terminating groups of adjacent layers of the $Ti_3C_2T_x$ MXene. Fascinatingly, it is observed that this H-bonding between hydroxyl (OH) and F/O groups is vital for maintaining the structural integrity and stability of the multilayer $Ti_3C_2T_x$ MXene and is a necessary factor in adhesion energy. Mainly, hydrogen bonds are formed between hydroxyl groups on one layer and fluorine or oxygen groups on neighboring layers of $Ti_3C_2T_x$ MXene, leading to an additional increase in the interlayer adhesion energy and improving the stability of the multilayer structure.

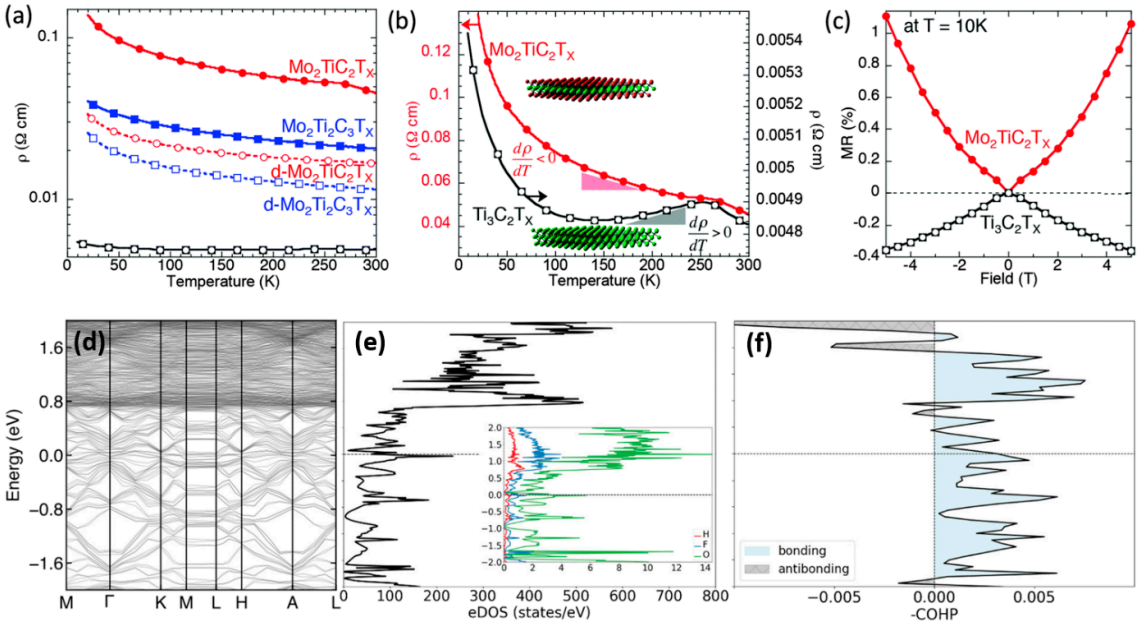


Figure 6. (**a**) The temperature-dependent resistivity ρ(T) plots of $Mo_2TiC_2T_x$ (red), $Mo_2Ti_2C_3T_x$ (blue), and $Ti_3C_2T_x$ (black) [delaminated films shown as dashed lines and pressed multilayered powders as solid lines]; (**b**) a comparison of the resistivity of $Mo_2TiC_2T_x$ (red) and $Ti_3C_2T_x$ (black), and the corresponding (**c**) measurements of the magnetoresistance as a function of the magnetic field at 10 K. Reproduced with permission from Ref. [113]. Copyright (2016) Royal Society of Chemistry. (**d**) The electronic band structure, (**e**) electronic density of states, and (**f**) -COHP of multilayer metallic $Ti_3C_2T_x$ MXene. Reproduced with permission from Ref. [114]. Copyright (2024) Royal Society of Chemistry.

Therefore, it is concluded from these optical, magnetic and electronic properties that MXenes could have a vital impact due to their gas sensing characteristics. Interestingly, the optical, magnetic, and electronic properties of $Ti_3C_2T_x$ MXene are deeply interconnected, providing synergistic effects, which enhances its gas sensing capabilities. NO_2 gas acts as an electron acceptor, reducing conductivity; however, reducing gases like NH_3 increase it by donating electrons. Furthermore, the surface terminations (-OH, -O, -F) of $Ti_3C_2T_x$ MXene significantly enhance its surface reactivity, providing active sites for gas adsorption. These terminations of $Ti_3C_2T_x$ MXene modify the density of states near the Fermi level, influencing the electronic response and enabling a high sensitivity to adsorbed gases. In addition, the optical properties also contribute significantly to the gas sensing capabilities of $Ti_3C_2T_x$ MXene. The material demonstrates surface plasmon resonance (SPR) in the visible and near-infrared regions, which can be modulated by changes in the local refractive index due to gas adsorption. This interaction causes shifts in the plasmonic response, enabling optical detection mechanisms. Fascinatingly, pristine $Ti_3C_2T_x$ MXene is typically non-magnetic; however, defects, gas adsorption, and specific functional groups can induce its magnetic properties. Adsorption of certain gases, such as O_2 and NO, can

generate localized magnetic moments and alter $Ti_3C_2T_x$ MXene's magnetic behavior. This gas-induced magnetism provides an additional pathway for gas sensing, where changes in magnetic properties can be detected using magnetoresistance. Therefore, it is concluded that the optical, magnetic, and electronic properties of $Ti_3C_2T_x$ MXene, combined with its 2D structure and tunable surface chemistry, make it a powerful material for gas sensing applications. Also, $Ti_3C_2T_x$ MXene's ability to detect gases through multiple mechanisms, such as changes in conductivity, optical shifts, and magnetic properties, offers a versatile platform for designing sensitive and selective sensors. Moreover, advancements in functionalization and defect engineering are expected to further enhance the potential of $Ti_3C_2T_x$ MXene in gas sensing technologies.

4. Gas Sensing Study

Due to their comparatively high surface area, metallic conductivity, and hydrophilicity, 2D MXenes and their hybrids have demonstrated great promise for NH_3 gas sensing applications, as discussed by Atkare et al. [115]. Their perspective only focuses on NH_3 detection based on 2D MXenes and their hybrids. Due to the existence of different functional groups (-O, -OH, and -F) on the surface of the MXenes, the gas molecules could interact with the MXenes via different mechanisms, such as hydrogen bonding, van der Waals forces, and electrostatic interactions. Radhakrishnan et al. discussed the recent progress in 2D MXenes for NO_2 gas sensing [116]. Their outlook only focuses on the NO_2 gas sensing properties, mechanism, and the role of doping and heterostructures of 2D MXenes. Interestingly, the doping and heterostructures of 2D MXenes offer interactions that influence the electrical properties of the MXenes and can be used to detect various gases. In addition, Zhang et al. discussed MXene-based gas sensors for the monitoring of food safety [117]. Their perspective only emphasizes the detection of volatile organic compounds such as hydrogen sulfide (H_2S), trimethylamine (TMA), acetone, and ethanol, which are critical for monitoring food quality and ensuring safety in agricultural products. These gases are typically released during the spoilage process, serving as key indicators of food degradation. Moreover, Ta et al. described a review of gas sensing and energy harvesting applications [118]. On the other hand, Yi et al. reported and focused only on the colorimetric detection of dipterex [119]. However, the present review focuses on the structural, morphological, optical, electronic, magnetic, and gas sensing properties of $Ti_3C_2T_x$ MXene.

4.1. H_2 Gas Sensing

The adsorption of hydrogen molecules on the surface of $Ti_3C_2T_x$ MXene leads to a change in its resistance and is attributed to the high sensitivity of H_2. Moreover, the response time of a $Ti_3C_2T_x$ MXene sensor is required in practical applications. The fast adsorption–desorption dynamics of H_2 are characteristic on the basis of the high conductivity of $Ti_3C_2T_x$ MXene, leading to high response and recovery times. Additionally, the selectivity of $Ti_3C_2T_x$ MXene is typically improved by surface functionalization or doping for H_2 over other gasses [120]. Strong gas sensing selectivity performance can be achieved by doping various elements/compounds into the $Ti_3C_2T_x$ MXene. In recent years, it was found that doping into $Ti_3C_2T_x$ MXene can enhance its sensitivity, selectivity, and stability. In addition, Pd is well known as an excellent catalytic with a strong hydrogen adsorption capability. The dissociation of hydrogen molecules on Pd sites on $Ti_3C_2T_x$ MXene improves its H_2 sensitivity, fast response, and selectivity. Research by Nam et al. demonstrated that Pd-functionalized $Ti_3C_2T_x$ MXene exhibited significantly improved H_2 sensing performance, with lower detection limits, selectivity, and quicker response times [121]. On the other hand, $Ti_3C_2T_x$ MXene@Pd has shown improved H_2 sensing performance, as reported by Zhu et al., where the sensor exhibited higher flexibility, sensitivity, and faster

recovery times compared to undoped $Ti_3C_2T_x$ MXenes [122]. Qui et al. discussed a 3D PdCu/$Ti_3C_2T_x$ MXene sensor, which demonstrated enhanced sensitivity and selectivity for H_2 at room temperature [123]. Significant advancements towards H_2 gas detection for energy systems and industrial safety are realized by the 3D PdCu-modified $Ti_3C_2T_x$ MXene sensor (PdCu/$Ti_3C_2T_x$). Interestingly, its unique architecture improves active site exposure and H_2 gas diffusion to enable a fast 4 s response time, ultra-low detection limit (0.1% H_2), and superior selectivity, stability, and repeatability. Moreover, by promoting synergistic interaction, the PdCu and $Ti_3C_2T_x$ MXene heterostructure improves performance.

Yang et al. discussed the H_2 gas sensing performance of Pd/$Ti_3C_2T_x$ sensors, as shown in Figure 7a–f [124]. Figure 7a,b show dynamic response–recovery curves, which indicate that the Pd/$Ti_3C_2T_x$ sensor shows reversible behavior when exposed to H_2. The Pd/$Ti_3C_2T_x$ sensors exhibit p-type semiconductor-like behavior when exposed to H_2 gas and have increased sensor resistance. After H_2 removal, the Pd/$Ti_3C_2T_x$ sensor heals to its baseline resistance, showing effective desorption and reversibility. Figure 7c quantifies the relationship between H_2 (100–500 ppm) concentration and the responses of the Pd/Ti_2CT_x and Pd/$Ti_3C_2T_x$ sensors. It is observed that there is nearly three times as much of a response, at 2.2%, to H_2 at 500 ppm for Pd/Ti_2CT_x compared to Pd/$Ti_3C_2T_x$, which had a response of 0.76%. Figure 7d displays the response and recovery times of the Pd/Ti_2CT_x and Pd/$Ti_3C_2T_x$ sensors at 200 ppm H_2. Fascinatingly, the Pd/Ti_2CT_x sensor illustrates significantly faster kinetics (100 s response and 710s recovery time) than the Pd/$Ti_3C_2T_x$ sensor (160 s response and 850 s recovery time). These superior interaction dynamics of the Pd/Ti_2CT_x heterointerface are also characteristic of a rapid response and recovery, marking the faster adsorption and desorption of hydrogen gas molecules. Figure 7e demonstrates the stability and reproducibility of the Pd/Ti_2CT_x sensor through repeated response–recovery cycles at 200 ppm H_2. These robust and reliable results of consistent Pd/Ti_2CT_x sensor responses over multiple cycles confirm its robustness and reliability for practical applications. In Figure 7f, the selectivity of the Pd/Ti_2CT_x and Pd/$Ti_3C_2T_x$ sensors is evaluated by comparing their responses to NH_3, CO, C_3H_6O, HCHO, C_2H_5OH, and H_2. The Pd/Ti_2CT_x exhibits the highest response to H_2 and thus demonstrates excellent selectivity for targeted gas detection applications. Therefore, it was concluded that the thinner structure of the Ti_2CT_x sensor is responsible for its superb H_2 gas sensing properties, which result from an increase in the specific surface area, more active sites for adsorption, and a more effective charge transfer at the Pd–MXene heterointerface.

4.2. NH_3 Gas Sensing

The development of a proton exchange membrane fuel cell (PEMFC) sensor based on Pt/$Ti_3C_2T_x$ MXene for the detection of ammonia (NH_3) has been studied [125]. Pt nanoparticles supported on Pt/$Ti_3C_2T_x$ MXene nanosheets show enhanced sensitivity (456 nA/ppm) over conventional Pt/C sensors (313 nA/ppm) at room temperature with a limit of detection (LoD) of as low as 15 ppb. This remarkable performance arises from two synergistic effects: (i) the intrinsic high corrosion resistance and electrical conductivity of $Ti_3C_2T_x$ ensures stable and efficient charge transfer, and (ii) the enhanced anchoring effect between Pt particles and the $Ti_3C_2T_x$ nanosheet reduces catalyst detachment and improves stability. As a result of these characteristics, the sensor provides exceptional selectivity, reproducibility, and long-term stability. Moreover, the fabrication of a SnO_2/$Ti_3C_2T_x$ heterojunction sensor for the sensing of ammonia (NH_3) gas has been studied [126]. The study develops SnO_2/$Ti_3C_2T_x$ heterojunction nanocomposites for highly efficient and reliable NH_3 detection at room temperature. It is observed the SnO_2/$Ti_3C_2T_x$ heterojunction sensor elucidates a higher response than the $Ti_3C_2T_x$ sensor due to the synergistic effects of the heterojunction interface, which promotes efficient charge transfer and gas

adsorption. Moreover, the $SnO_2/Ti_3C_2T_x$ heterojunction sensor's high sensitivity is further evidenced by the detection of NH_3 at the ppb level, which makes it an attractive candidate for environmental monitoring and industrial safety. Fascinatingly, by combining the gas sensing properties of SnO_2 with the surface porosity and the few lamellar structures of $Ti_3C_2T_x$, this combination is uniquely sensitive to NH_3 gas molecule capture and release. Most interestingly, the $SnO_2/Ti_3C_2T_x$ heterojunction sensor runs at room temperature. Therefore, it does not consume additional external heating which greatly contributes to lower energy expenditure. The combination of these features fits well with the worldwide movement towards energy-efficient technologies. The $SnO_2/Ti_3C_2T_x$ heterojunction sensor shows high sensitivity, fast response and recovery times, and excellent selectivity and stability. In addition, the $SnO_2/Ti_3C_2T_x$ heterojunction sensor's ability to select NH_3 from other gases addresses a common problem with gas sensing technologies. Interestingly, the $GaN/Ti_3C_2T_x$ composite was synthesized via hydrothermal and nitridation processes, integrating the high conductivity of $Ti_3C_2T_x$ MXene with the excellent sensing properties of GaN nanorods [127]. This innovative combination achieves improved NH_3 sensing performance at room temperature, solving the high-temperature limitation of GaN nanorods. At room temperature, the $GaN/Ti_3C_2T_x$ composite sensor demonstrates a lower detection limit of 0.5 ppm and a response 3.4 times higher than $Ti_3C_2T_x$ alone. However, this study does not address the cost and scalability issues of mass production. In addition, work at extreme conditions, including RH > 80% or varying temperatures, is unexplored. The gas sensing mechanism for other gases is also not fully discussed. Stimulatingly, the use of self-assembled $Ti_3C_2T_x$ MXene thin films as high-performance NH_3 sensors has been explored [128]. In this study, the development of a high-performance NH_3 gas sensor using $Ti_3C_2T_x$ MXene nanosheet thin films grown by enhanced interfacial self-assembly is investigated. Ultra-thin films (<10 nm thick) with excellent sensitivity (1.92% at 1 ppm NH_3), a response time of 179 s, and a recovery time of 612 s at room temperature result from this. Despite the occurrence of a variety of chemical changes related to humidity variation (10% to 90% RH), the $Ti_3C_2T_x$ MXene thin-film sensor maintained remarkably stable performance and reproducible measures throughout wide humidity levels, suitable for environmental monitoring and other practical applications. The $Ti_3C_2T_x$ MXene thin-film sensor shows superior sensitivity to low concentrations of ammonia (1 ppm) and rapid response and recovery times. It works without requiring a high-temperature heating element and reduces energy use at room temperature. Such a fabrication process is scalable and cost-effective, potentially resulting in large-scale productions. Remarkably, one study discusses the use of α-$Fe_2O_3/Ti_3C_2T_x$ MXene nanocomposites to detect NH_3 at room temperatures in a high-performance NH_3 sensor [129]. Because of their hierarchical nanostructures achieved by a single hydrothermal method, these α-$Fe_2O_3/Ti_3C_2T_x$ MXene composites have high sensitivity to NH_3 (18.3% for 5 ppm at room temperature), fast response and recovery (<2.5 s), good reversibility, and good stability. The plausible NH_3 sensing mechanism is supported by density functional theory (DFT) calculations that reveal a strong adsorption capacity and high gas selectivity. The results present the unique hierarchical structure of α-Fe_2O_3 nanoflower features and $Ti_3C_2T_x$ MXene sheets' hybrid heterojunctions that improve NH_3 gas sensing properties at room temperature. More investigation is needed to determine the stability and compatibility of the α-$Fe_2O_3/Ti_3C_2T_x$ MXene composite in practical applications, such as wearable devices, and under variable environmental conditions.

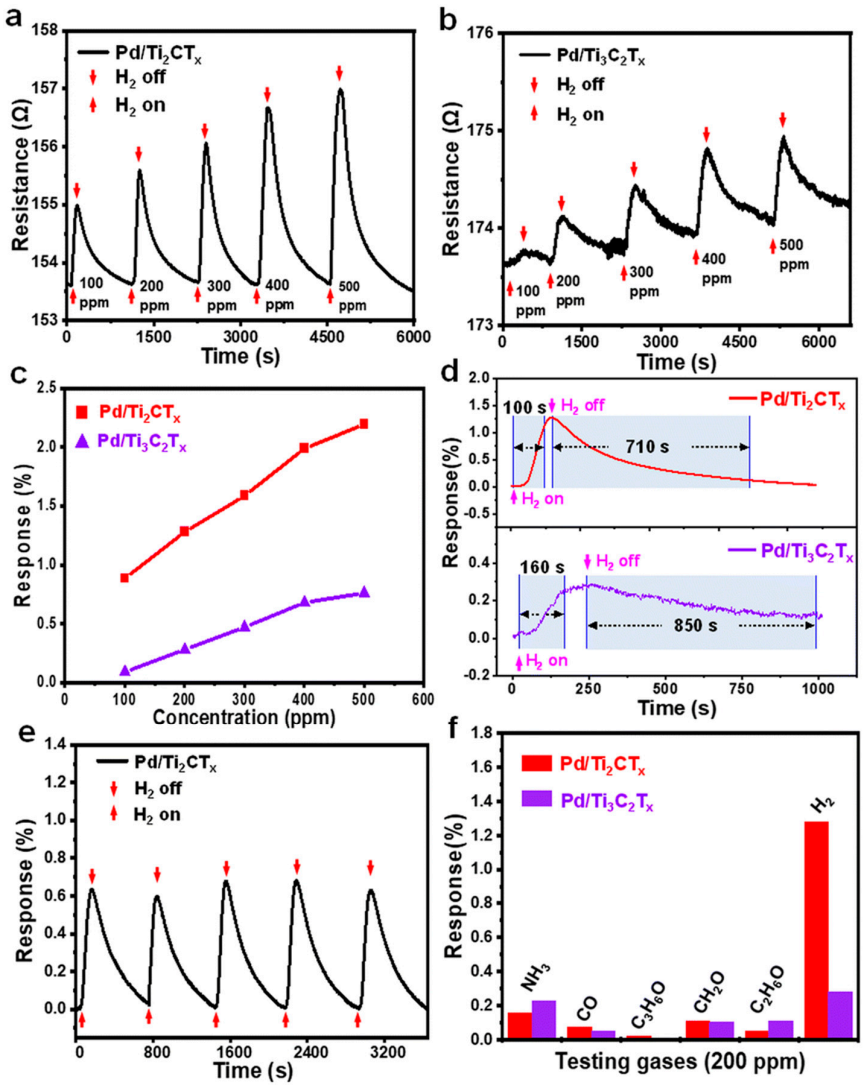


Figure 7. (**a**) Dynamic response–recovery curves of Pd/Ti_2CT_x and (**b**) $Pd/Ti_3C_2T_x$ sensors to varying concentrations of H_2 at room temperature. (**c**) Correlation between H_2 concentration and response for Pd/Ti_2CT_x and $Pd/Ti_3C_2T_x$ sensors. (**d**) Extracted response and recovery times from the response–recovery curves of Pd/Ti_2CT_x and $Pd/Ti_3C_2T_x$ sensors at 200 ppm of H_2. (**e**) Cycling response–recovery curves of Pd/Ti_2CT_x sensor at 200 ppm of H_2. (**f**) Selectivity test results of Pd/Ti_2CT_x and $Pd/Ti_3C_2T_x$ sensors. Reproduced with permission from Ref. [124]. Copyright (2023) Royal Society of Chemistry.

Ranjith et al. discussed the NH_3 gas sensing performance of a $Pt@SnS_2/Ti_3C_2T_x$ MXene sensor, as revealed in Figure 8a–e [130]. Figure 8a shows a schematic representation of the gas sensing mechanism of the $Pt@SnS_2/Ti_3C_2T_x$ MXene sensor under the presence of humidity. By avoiding the adverse effects of water molecules on the sensing surface, the TES-functionalized $Pt@SnS_2/Ti_3C_2T_x$ MXene sensor displays a strategic design. TES functionalization, which gives it a hydrophobic nature, is such that there is no or very little interaction of water with the TES-functionalized $Pt@SnS_2/Ti_3C_2T_x$ MXene sensor's active surface. Therefore, it is concluded that the TES-functionalized $Pt@SnS_2/Ti_3C_2T_x$ MXene sensor has a sufficiently high sensitivity and reliability even in a highly humid environment, which is a challenging matter for conventional sensors. Figure 8b depicts the response curves of the TES_4-$Pt@SnS_2/Ti_3C_2T_x$ MXene sensor towards 10 ppm of NH_3 within a range of relative humidity (RH) levels (9%, 27%, 38%, 53%, 74%, and 92%). The TES_4-$Pt@SnS_2/Ti_3C_2T_x$ MXene sensor reveals a reasonably retained response to a fairly wide humidity range. Figure 8c depicts the SRH_0/SRH ratio vs. humidity plots of the

TES_4-Pt@SnS_2/$Ti_3C_2T_x$ MXene gas sensor. The TES-functionalized TES_4-Pt@SnS_2/$Ti_3C_2T_x$ MXene sensor displays a stable SRH_0/SRH ratio, confirming minimal degradation of performance with increasing RH. This stability demonstrates that TES functionalization can suppress humidity-induced interference. Figure 8d illustrates the RSD values of the TES_4-Pt@SnS_2/$Ti_3C_2T_x$ MXene and Pt@SnS_2/$Ti_3C_2T_x$ MXene sensors. Its reliability and constant function under varying humidity conditions are better represented in the RSD values of the TES_4-Pt@SnS_2/$Ti_3C_2T_x$ MXene sensor. Figure 8e shows the long-term stability of the TES_4-Pt@SnS_2/$Ti_3C_2T_x$ MXene and Pt@SnS_2/$Ti_3C_2T_x$ MXene sensors. In long-term applications, the TES_4-Pt@SnS_2/$Ti_3C_2T_x$ MXene sensor remains responsive with minimal loss. On the other hand, the Pt@SnS_2/$Ti_3C_2T_x$ MXene sensor with non-functionalized Pt shows more severe degradation over time. Therefore, it is concluded that the TES_4-Pt@SnS_2/$Ti_3C_2T_x$ MXene exhibits excellent NH_3 detection under a wide range of challenging humidity conditions. Interestingly, TES functionalization incorporation in the TES_4-Pt@SnS_2/$Ti_3C_2T_x$ MXene sensor notably enhances humidity tolerance, stability, and overall sensing reliability, thereby becoming a very promising candidate for real-world applications.

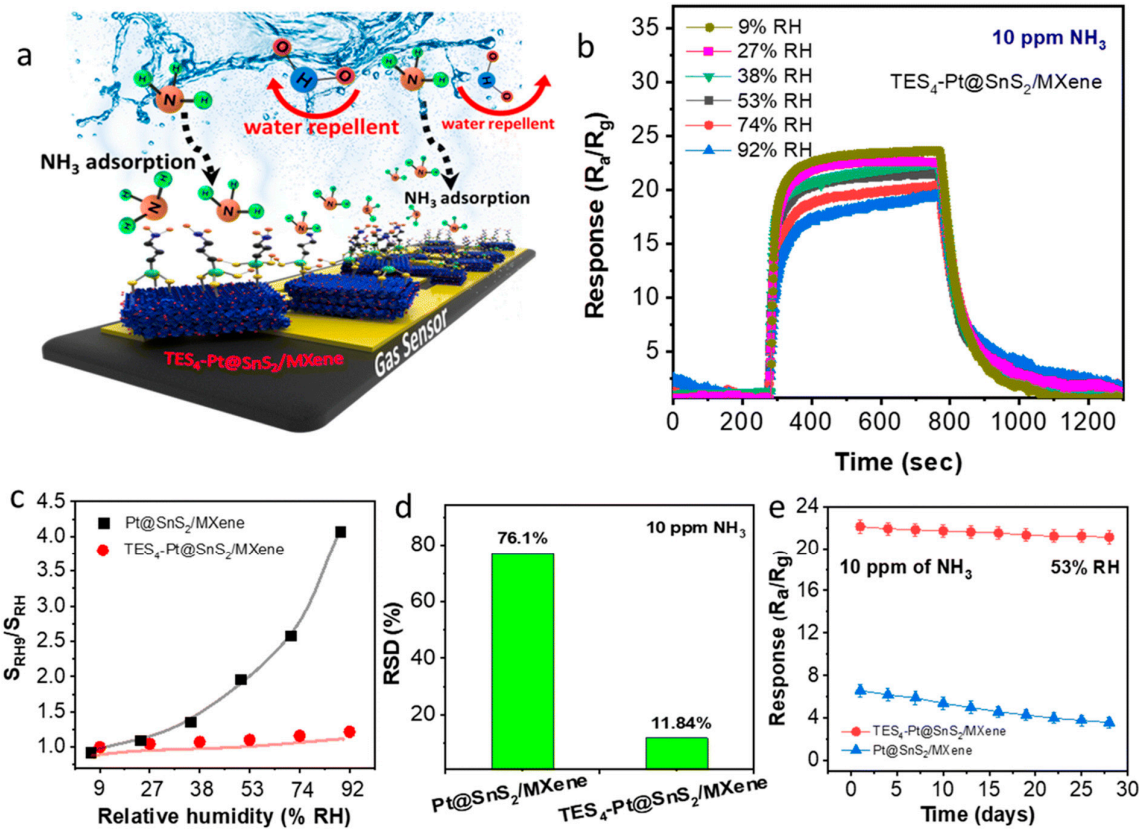


Figure 8. (**a**) A clear and detailed diagram of the gas sensing mechanism of the TES_4-Pt@SnS_2/$Ti_3C_2T_x$ MXene sensor in the existence of humidity. (**b**) The response curves of the TES_4-Pt@SnS_2/$Ti_3C_2T_x$ MXene sensor to 10 ppm NH_3 under varying RHs. (**c**) The variation of S_{RHO}/S_{RH} with relative humidity. (**d**) The RSDs (%) of the Pt@SnS_2/$Ti_3C_2T_x$ MXene and TES_4-Pt@SnS_2/$Ti_3C_2T_x$ MXene sensors. (**e**) The stability of the Pt@SnS_2/$Ti_3C_2T_x$ MXene and TES_4-Pt@SnS_2/$Ti_3C_2T_x$ MXene sensors over 30 days at 10 ppm of NH_3. Reproduced with permission from Ref. [130]. Copyright (2024) Royal Society of Chemistry.

4.3. VOCs Gas Sensing

The recent literature highlights the exceptional potential of $Ti_3C_2T_x$ MXenes for VOC sensing. The metallic $Ti_3C_2T_x$ MXene sensor discussed by Kim et al. showed enhanced sensitivity and selectivity for VOC sensing [93]. This work is significant as it addresses a critical

challenge in solid-state gas sensing based on the $Ti_3C_2T_x$ MXene sensor, providing ultra-high sensitivity for detecting volatile organic compounds (VOCs) at the parts-per-billion (ppb) level. The feasible applications of VOC sensing include environmental monitoring or the early detection of diseases, where trace-level sensitivity can be life-saving. The sensor operates with high metallic conductivity, low electrical noise, and a fully functionalized surface of $Ti_3C_2T_x$ MXene for an unprecedented detection limit of 50–100 ppb for VOCs at room temperature. Furthermore, the $Ti_3C_2T_x$ MXene sensor exceeds conventional semiconductor-based sensors regarding signal-to-noise ratio, with a result which is two orders of magnitude higher than in other 2D materials. The findings are critical to using functionalized metallic $Ti_3C_2T_x$ MXene for ultra-sensitive sensing. Bhardwaj et al. discussed VOC detection based on a $SrTiO_3$-passivated $Ti_3C_2T_x$ MXene sensor [131]. In this study, a novel way to enhance the humidity tolerance of $Ti_3C_2T_x$ MXene-based sensors for volatile organic compound (VOC) sensing is presented by passivating the hydrophilic $Ti_3C_2T_x$ MXene surface with a superhydrophobic $SrTiO_3$ (STO) overlayer. Interestingly, the sensing properties of $Ti_3C_2T_x$ MXenes are combined with the moisture-blocking properties of STO, a known hydrophobic perovskite. From an application point of view, this approach reduces humidity interference, a significant problem in gas sensing applications. The $SrTiO_3$-passivated $Ti_3C_2T_x$ MXene sensor exhibits good selectivity, repeatability, and long-term stability, with a detection limit (LOD) down to 40 ppb. These features offer promise for real-time VOC detection using an $SrTiO_3$-passivated $Ti_3C_2T_x$ MXene sensor. Overall, this work provides a scientifically sound strategy to improve the humidity tolerance of $SrTiO_3$-passivated $Ti_3C_2T_x$ MXene-based VOC sensors. Tian et al. discussed the ethanol gas sensing properties of a carbon quantum dots (CQDs)-sensitized $Ti_3C_2T_x$ MXene sensor [132]. Integrating $Ti_3C_2T_x$ MXene and carbon quantum dots (CQDs) into a composite, which exploits the photoresponsive properties of CQDs and high conductivity of $Ti_3C_2T_x$ MXene, is the novelty of the composite. Its improved specific surface area, charge transfer, and photoelectronic properties result in the increased detection of ethanol by using the CQDs/$Ti_3C_2T_x$ MXene sensor. Also, the study signifies the roles of ultraviolet (UV) irradiation in improving CQDs/$Ti_3C_2T_x$ MXene sensor efficiency by reducing recovery time. The practicality of the CQDs/$Ti_3C_2T_x$ MXene sensor's requirement of a specific operating temperature (140 °C) may increase energy consumption, making it less environmentally friendly. In addition, while UV irradiation will shorten recovery time, the dependence on UV light may restrict its utility in low light or off-grid conditions. Song et al. reported the HCHO and triethylamine gas sensing properties of a ZnO/$Ti_3C_2T_x$ MXene heterostructure sensor [133]. A scientifically robust approach to developing formaldehyde and trimethylamine sensing performance utilizing a ZnO/$Ti_3C_2T_x$ MXene heterostructure sensor is presented and shown to be successful in measuring the critical indicators of seafood freshness. The ZnO/$Ti_3C_2T_x$ MXene heterostructure sensor's versatility demonstrated in its response to formaldehyde at room temperature and triethylamine under thermal conditions is remarkable. However, some limitations exist, such as external light activation and temperature adjustment for specific gas detection, its performance at lower concentrations below 100 ppm or in real-world mixed gas detection, and the fact the thermal energy required for triethylamine sensing may impair its usefulness in energy-restricted environments. Song et al. reported n-butanol recognition using an Fe_2O_3/$Ti_3C_2T_x$ MXene heterostructure sensor [134]. Interestingly, Schottky heterojunctions and synergistic effects were found in the gas sensing performance of the innovative n-type Fe_2O_3 nanoparticles/n-type $Ti_3C_2T_x$ MXene sensor. The Fe_2O_3/$Ti_3C_2T_x$ MXene heterostructure sensor performs better due to its high conductivity, allowing for the faster transfer of carriers and a reduction in resistance, and abundant surface defects that boost the adsorption and reaction of gas molecules. Furthermore, the study delivers a roadmap to constructing a gas-sensitive

$Fe_2O_3/Ti_3C_2T_x$ MXene heterostructure sensor to detect ppb-level gas. Nevertheless, its drawbacks may be synthesis difficulties in preparing $Fe_2O_3/Ti_3C_2T_x$ MXene heterostructures on a large scale because of the possible degradation of $Ti_3C_2T_x$ MXene under some environmental conditions.

Yao et al. reported isopropanol detection at room temperature using an $MoO_3/TiO_2/Ti_3C_2T_x$ nanocomposite sensor, as depicted in Figure 9a–h [135]. Figure 9 also shows the comprehensive performance evaluation of the $MoO_3/TiO_2/Ti_3C_2T_x$ (MTT3) composite-based gas sensor for isopropanol detection. Figure 9a illustrates multiple exposures of the sensor to 5 ppm isopropanol, during which it displays a stable response of approximately 45% in all cycles with repeatability. Figure 9b shows a remarkable response time of 33 s and a recovery time of 8 s for the MTT3 sensor for 5 ppm isopropanol. Figure 9c,d depict the dynamic response curves of the MTT3 sensor with varying isopropanol concentrations, revealing a linear relationship between the response and isopropanol concentration, confirming the MTT3 sensor's sensitivity and precision. Interestingly, 50.45 ppb is the limit of detection (LOD), and 168.17 ppb is the limit of quantification (LOQ), demonstrating the MTT3 sensor's ability to detect trace levels of isopropanol. Figure 9e exhibits the 50 ppm isopropanol testing results of the MTT3 sensor over 30 days, elucidating brilliant stability. Figure 9f further demonstrates the MTT3 sensor's selectivity capability in distinguishing other potential interfering gases. Selectivity is a crucial characteristic because, in complex environments, multiple VOCs are present, which requires a suitable detection of desired gas. Figure 9g,h display that the MTT3 sensor's performance degraded with varying humidity levels. However, above 80% RH, the MTT3 sensor's response was reduced, possibly due to water vapor interference. Also, it was found that the MTT3 sensor's performance returned to baseline after exposure to lower humidity, thereby showing the reversibility. Interestingly, the MTT3 sensor demonstrates high sensitivity, fast response and recovery, long-term stability, and good selectivity toward isopropanol detection at room temperature.

4.4. NO_2 Sensing

$Ti_3C_2T_x$ MXene has gained significant attention in the research community for its potential applications in gas sensing, particularly for nitrogen dioxide (NO_2) detection. Gua et al. discussed NO_2 sensing based on a $Ti_3C_2T_x$ MXene/CuO nanocomposite sensor [136]. The advantages of the $Ti_3C_2T_x$ MXene/CuO nanocomposite sensor are its enhanced sensitivity to NO_2, significantly faster response–recovery dynamics, and long-term robust operation. In addition, the uniformity of the performance of the $Ti_3C_2T_x$ MXene/CuO nanocomposite sensor has not been studied for gases other than NO_2, which impedes its potential utility. However, the $Ti_3C_2T_x$ MXene/CuO nanocomposite sensor still overcomes the challenges of room-temperature NO_2 gas sensing technology. Shin et al. discussed NO_2 detection based on a ZnO-$Ti_3C_2T_x$ MXene nanocomposite sensor [137]. Under the influence of microwave irradiation for 1–8 min, the NO_2 sensing performance of ZnO-$Ti_3C_2T_x$ MXene nanocomposites with varying $Ti_3C_2T_x$ MXene contents was studied. The superiority in NO_2 response over some conventional materials was attributed to the creation of ZnO-$Ti_3C_2T_x$ MXene Schottky barriers, microwave-induced oxygen vacancies, a large surface area, and functional surface groups on $Ti_3C_2T_x$ MXene. In addition, the sensor exhibited high reproducibility and repeatability over a six-month period, which indicates great potential for practical application. Furthermore, $Ti_3C_2T_x$ MXene-functionalized materials may be degraded in prolonged exposure to high temperatures; however, this study shows that microwave-irradiated ZnO-$Ti_3C_2T_x$ MXene nanocomposites hold the potential to be cost-effective and stable NO_2 sensing applications. Tang et al. discussed NO_2 sensing based on an M-$Ti_3C_2T_x$ MXene sensor [138]. Using a molten salt immersion method, this study successfully modulates the intrinsic functional groups of $Ti_3C_2T_x$ MX-

ene. To overcome the high room-temperature NO_2 detection limit, the sensor is introduced to tunable oxygen-functionalized surfaces. These modifications include O addition to surface titanium atoms and O substitution on edge carbon atoms to maximize -O functional groups and enhance gas sensing performance. DFT calculations verify the covalent bond formation between the -O group and NO_2 gas molecules, enhancing adsorption capacity. Hu et al. discussed NO_2 sensing based on a $Ti_3C_2T_x/TiO_2/Au$ heterostructure sensor [139]. Here, a visible light-assisted gas sensor based on $Ti_3C_2T_x/TiO_2/Au$ heterostructures for room-temperature detection with an extremely low detection limit of NO_2 was studied. The $Ti_3C_2T_x/TiO_2/Au$ heterostructure sensor displays superior performance, with sensitivity without light illumination. The $Ti_3C_2T_x/TiO_2/Au$ heterostructure sensor unveils the theoretical and experimental investigations of localized surface plasmon resonance (LSPR) and localized photothermal effects to increase photon utilization and NO_2 gas-sensitive reactions. Interestingly, Au nanoparticles are incorporated to enhance the sensitivity and selectivity of NO_2 detection. Quick response and recovery times make the $Ti_3C_2T_x/TiO_2/Au$ heterostructure sensor more suitable for real-time monitoring, a key requirement for Internet of Things (IoT) applications. The cost-effective, large-scale production of $Ti_3C_2T_x/TiO_2/Au$ heterostructure sensors may be complicated by their complex fabrication process. In addition, this work demonstrates the potential of plasmonic photothermal sensitization to move gas sensor technologies toward their IoT applications.

Liu et al. reported NO_2 gas sensing properties at room temperature using a $Ti_3C_2T_x@TiO_2@MoS_2$ heterostructure sensor, as described in Figure 10a–f [140]. As shown in Figure 10, the $Ti_3C_2T_x@TiO_2@MoS_2$ heterostructure sensor performs exceptionally well at NO_2 detection at ambient temperatures. Figure 10a is the dynamic response of the $Ti_3C_2T_x@TiO_2@MoS_2$ heterostructure sensor to varying concentrations of NO_2. When exposed to NO_2 gas, the $Ti_3C_2T_x@TiO_2@MoS_2$ heterostructure sensor exhibits a rapid decrease in resistance, a characteristic behavior of a p-type semiconductor. To explore the $Ti_3C_2T_x@TiO_2@MoS_2$ heterostructure sensor's sensitivity to NO_2, Figure 10b displays the magnitude of responses of different sensors ($TiO_2@MoS_2$, $Ti_3C_2T_x@MoS_2$, and $Ti_3C_2T_x@TiO_2@MoS_2$) to 50 ppm of NO_2. Figure 10c,d show the $Ti_3C_2T_x@TiO_2@MoS_2$ heterostructure sensor's speed in detecting and recovering from NO_2 exposure. In addition, the $Ti_3C_2T_x@TiO_2@MoS_2$ heterostructure sensor demonstrates a significantly higher NO_2 sensing performance, which is attributed to the high conductivity of $Ti_3C_2T_x$ but also to the intimate contact at the heterointerfaces allowing for fast electron transfer and efficient gas adsorption–desorption kinetics. As illustrated in Figure 10e, the selectivity of the $Ti_3C_2T_x@TiO_2@MoS_2$ heterostructure sensor to NO_2 over other gases, including H_2, CO, CH_4, NH_3, and H_2S, is remarkable. Figure 10f depicts the stability of the $TiO_2@MoS_2$, $Ti_3C_2T_x@MoS_2$, and $Ti_3C_2T_x@TiO_2@MoS_2$ heterostructure sensors. It is observed that the sensors illustrate stability for up to eight weeks and five repeated tests for 50 ppm NO_2. This stability reflects the stiffness of the electronic properties and the sensor's structure, which indicates good long-term performance.

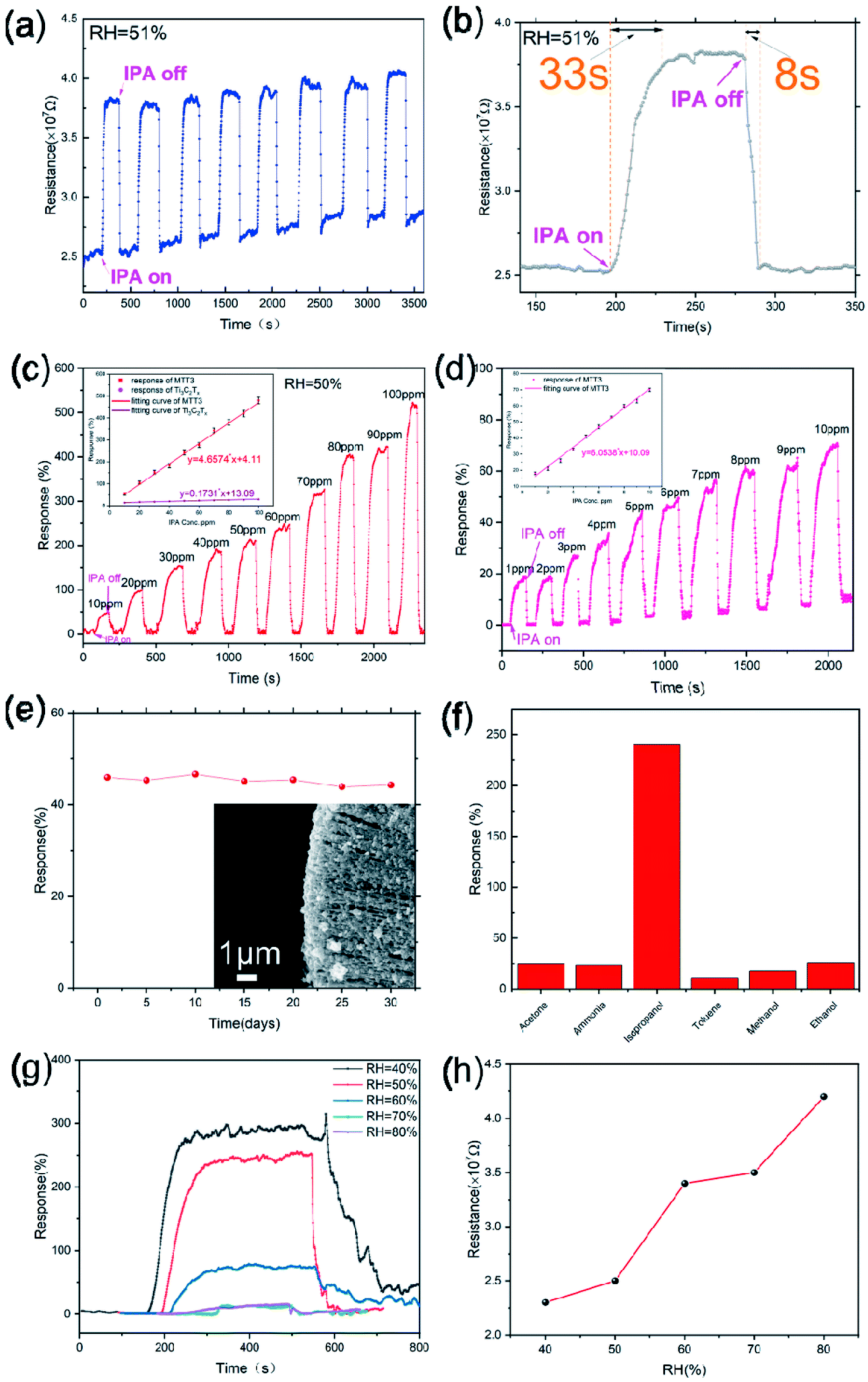


Figure 9. (**a**) The repeatability of the $MoO_3/TiO_2/Ti_3C_2T_x$ ternary (MTT3) composite sensor for detecting 5 ppm isopropanol; (**b**) the response and recovery times of the MTT3 composite sensor for 5 ppm isopropanol; (**c**) the response–recovery curves of the MTT3 composite sensor for isopropanol concentrations of 10, 20, 40, and 100 ppm at 50% relative humidity; (**d**) the response–recovery curves of the MTT3 composite sensor for isopropanol at low concentrations ranging from 1 ppm to 10 ppm; (**e**) the long-term stability of the MTT3 composite sensor for measuring 5 ppm isopropanol for approximately 30 days; (**f**) the selectivity of the MTT3 composite sensor to various gases with a concentration of 50 ppm; (**g**) the dynamic response–recovery curves of the MTT3 composite sensor for isopropanol at concentrations of 50 ppm in relative humidity levels of 40 to 80%; and (**h**) the baseline resistance of the MTT3 composite sensor over a range of relative humidity levels 40–80%. Reproduced with permission from Ref. [135]. Copyright (2022) Royal Society of Chemistry.

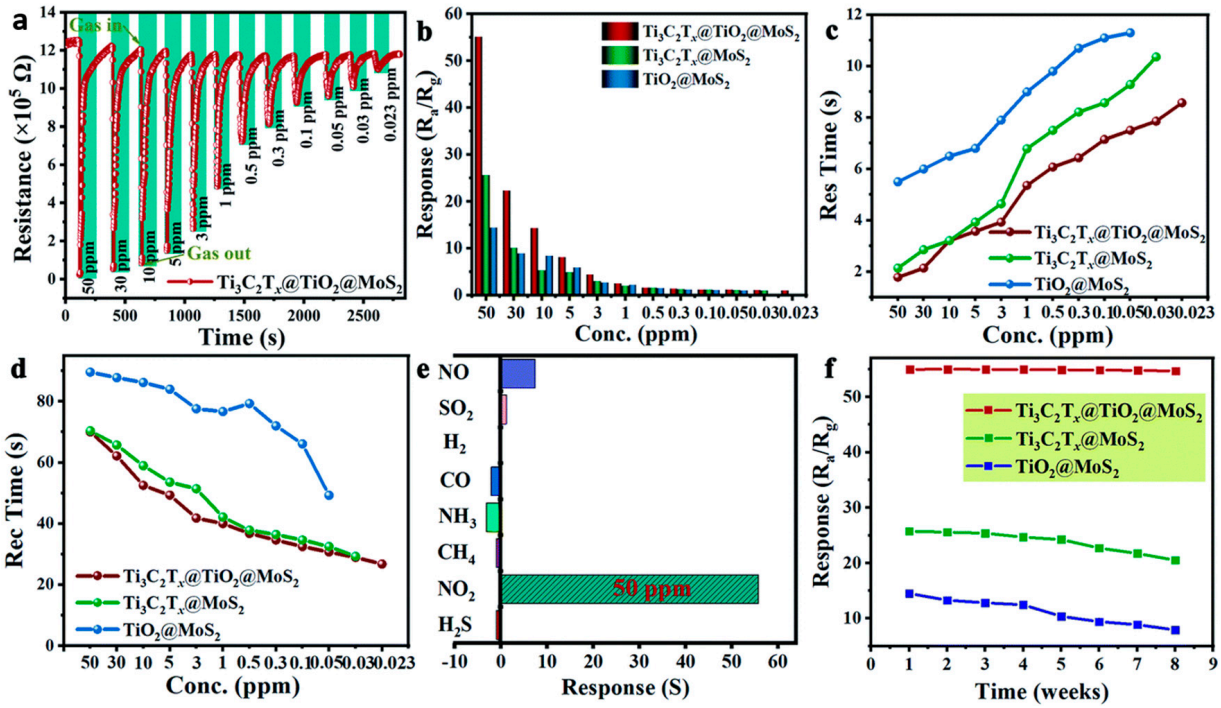


Figure 10. (**a**) Transient response curves of $Ti_3C_2T_x$@TiO_2@MoS_2 sensor to NO_2 at room temperature (RH = 23.4%). (**b**) Variation in response with concentration plot of TiO_2@MoS_2, $Ti_3C_2T_x$@MoS_2, and $Ti_3C_2T_x$@TiO_2@MoS_2 sensors. (**c**,**d**) Response time vs. concentration plots of TiO_2@MoS_2, $Ti_3C_2T_x$@MoS_2, and $Ti_3C_2T_x$@TiO_2@MoS_2 sensors. (**e**) Selectivity performance of $Ti_3C_2T_x$@TiO_2@MoS_2 sensor. (**f**) Stability of TiO_2@MoS_2, $Ti_3C_2T_x$@MoS_2, and $Ti_3C_2T_x$@TiO_2@MoS_2 sensors at 50 ppm NO_2. Reproduced with permission from Ref. [140]. Copyright (2022) Royal Society of Chemistry.

4.5. Humidity Sensing

Liu et al. propose a novel optical fiber relative humidity (RH) sensor using a tapered no-core fiber (TNCF) coated with $Ti_3C_2T_x$ MXene [141]. The $Ti_3C_2T_x$ MXene's refractive index (RI) changes upon RH variations, allowing it to sense humidity by shifting the transmission spectrum. The advantages of the $Ti_3C_2T_x$ MXene/TNCF sensor include a simple design, low cost, high reversibility, and excellent stability. A novel approach to optical fiber-based humidity sensing is demonstrated by the proposed sensor, exhibiting high sensitivity and fast response. Waheed et al. propose a novel 2D $Ti_3C_2T_x$ MXene nanosheet and graphene oxide sensor for humidity sensing [142]. A novel, high-performance, and cost-effective humidity sensor was developed using 2D $Ti_3C_2T_x$ MXene nanosheets as electrodes and graphene oxide (GO) as the sensing layer. The sensor device demonstrates rapid response and recovery times of 0.8 s and 0.9 s, respectively, while maintaining stability over 24 h. Density functional theory (DFT) simulations provided atomic-level insights into the humidity sensing mechanism, highlighting the formation of physical bonds between water molecules' hydrogen atoms and the oxygen atoms in the OH groups of the GO. The findings underscore the potential of 2D material-based sensors for low-cost, flexible, and highly sensitive humidity detection. This study contributes to advancing 2D materials in sensor technology, offering promising implications for diverse humidity sensing applications. In addition, Yu et al. propose a novel $Ti_3C_2T_x$ MXenes–RGO sensor for humidity sensing [143]. Based on the developed $Ti_3C_2T_x$ MXenes–RGO sensor, the prospects for achieving a highly sensitive and accurate biosensor for respiratory moisture diagnostics in real-time have been successful. This idea could dramatically change the axis of health diagnostics, where respiratory patterns could be scanned without physical contact, and it could further enhance

the sphere of environmental monitoring. Based on the results presented in the study, the $Ti_3C_2T_x$ MXenes–RGO sensor could point in the direction of new techniques with higher non-invasiveness in healthcare and environmental science. In addition, Tang et al. propose a novel C_{60}-OH/$Ti_3C_2T_X$ nanocomposite sensor for humidity sensing [144]. Incorporating C_{60}-OH with $Ti_3C_2T_X$ nanostructures in high-frequency quartz crystal microbalance (QCM) sensors may enhance their moisture adsorption capacity and sensitivity, as well as response and recovery rates. This approach can benefit the humidity sensing profiles that need greater sensitivity and time responsiveness, like human noninteraction.

Han et al. propose a novel $Ti_3C_2T_x$ MXene/SnO_2 heterostructure sensor for humidity sensing, depicted in Figure 11a–f [145]. The real-time resistance response of the $Ti_3C_2T_x$ MXene/SnO_2 heterostructure sensor during respiration in different rhythms and techniques is shown in Figure 11a,b in fast (30 bpm), normal (15 bpm), and slow (10 bpm) respiration. The study evidences the capability of the $Ti_3C_2T_x$ MXene/SnO_2 heterostructure sensor to distinguish between mouth and nose breathing. The research established that mouth breathing produces a lower resistance than nasal breathing, a factor attributed to the high humidity of the air leaving the mouth. These outcomes suggest the sensor's capability for continuous respiratory monitoring, which would be very helpful when diagnosing sleep and other respiratory disorders. Figure 11c shows the schematic depiction of the contactless gesture monitoring process of the $Ti_3C_2T_x$ MXene/SnO_2 heterostructure sensor. Figure 11d displays the transient resistance characteristics of the $Ti_3C_2T_x$ MXene/SnO_2 heterostructure sensor. Interestingly, if a finger is moved closer to the sensor, the resistance changes, going to a higher resistance level if it moves closer to the sensor within a limit of 1–4 mm. This change in resistance is due to a shift in humidity from the original humidity caused by the evaporation of sweat. This capability reveals that the sensor is capable of sensing the proximity of an object without actually touching it, creating an avenue for ingenious touchless interfaces as well as progressive human–machine interaction. Figure 11e portrays a photograph of a printed $Ti_3C_2T_x$ MXene/SnO_2 heterostructure sensor array to visualize the sensor. Figure 11f describes the response results of the printed $Ti_3C_2T_x$ MXene/SnO_2 heterostructure sensor array. The $Ti_3C_2T_x$ MXene/SnO_2 heterostructure sensor array can recognize localized changes in resistance when a finger is in proximity to some of these specific positions, as shown in Figure 11e. This capability demonstrates the potential uses of large-area humidity mapping in environmental sensing, gesture-based systems, and high-precision industrial control.

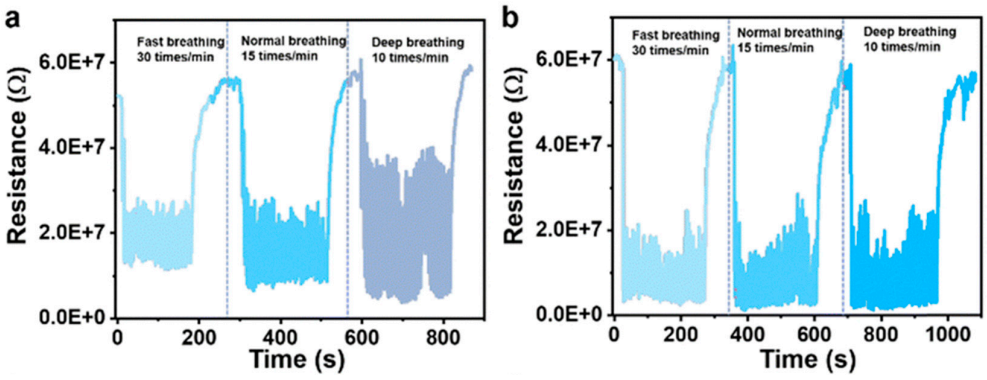


Figure 11. *Cont.*

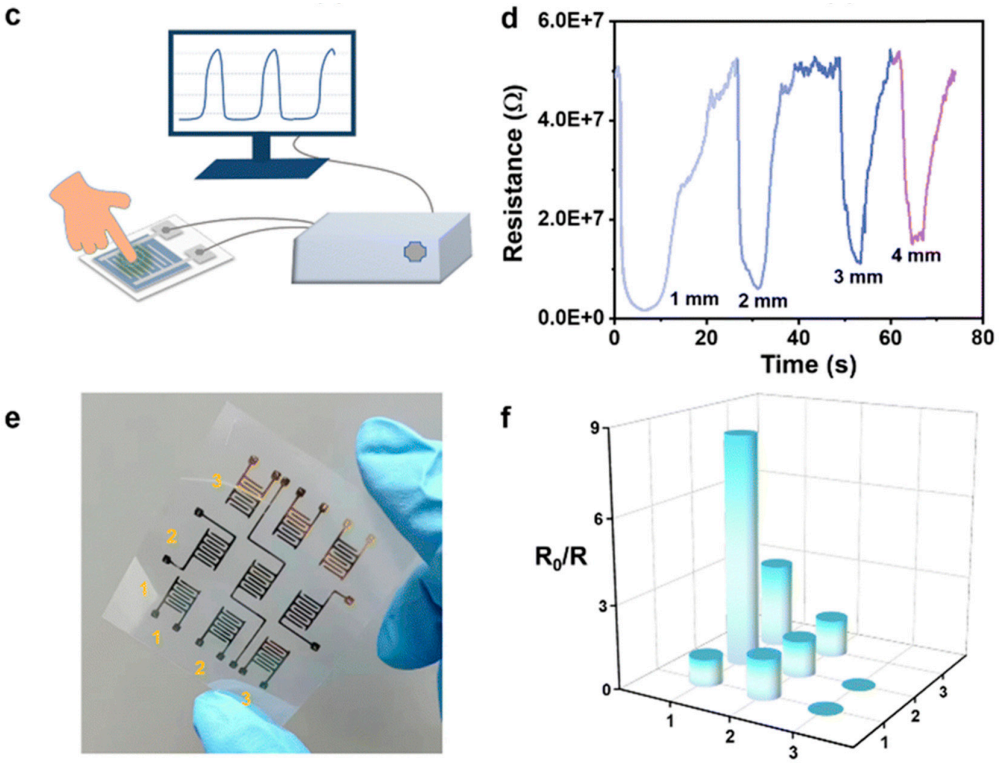


Figure 11. The $Ti_3C_2T_x/SnO_2$ sensor exhibits characteristic resistance responses to human breathing through the (**a**) nose and (**b**) mouth. (**c**) The graphic scheme of non-contact gesture monitoring. (**d**) The real-time resistance varies as a function of distance of 1–4 mm between a finger and the $Ti_3C_2T_x/SnO_2$ sensor. (**e**) A photograph of the printed $Ti_3C_2T_x/SnO_2$ sensor array shows its compact and potentially scalable design. (**f**) Testing of the $Ti_3C_2T_x/SnO_2$ sensor array is conducted, and the results confirm its practicality. Reproduced with permission from Ref. [145]. Copyright (2024) Royal Society of Chemistry.

5. Conclusions

$Ti_3C_2T_x$ MXene is a promising material for next-generation gas sensors, owing to its excellent intrinsic properties of high electrical conductivity, large specific surface area, and tunable surface chemistry. With these characteristics, $Ti_3C_2T_x$ MXene is suitable for gas sensing with high gas selectivity and sensitivity. By synthesizing, functionalizing, and integrating $Ti_3C_2T_x$ MXene into gas sensing devices, recent advances have shown the potential of this material to achieve both fast response times and further enhanced performance through composite device formation.

5.1. Current Limitations and Challenges

Although much progress has been made so far in designing and fabricating stable and reproducible $Ti_3C_2T_x$ MXene-based gas sensors, there are still significant hurdles to overcome in order to ensure sensor stability and reproducibility for the long term. However, despite these issues, such materials have not been widely adopted due to such factors as oxidative degradation, sensitivity to humidity, and differences in material quality. Beyond that, there are critical bottlenecks regarding the scalability of production methods and seamless integration with existing technologies to one another and the rest of the world.

5.2. Future Directions for Research and Development

To overcome these limitations and enable the commercialization of $Ti_3C_2T_x$ MXene gas sensors, the following strategies are proposed: (i) establish methods for synthesis that are both scalable and economical and also deposit consistent material quality and

yield; (ii) optimize the etching process as well as exploring other routes to produce $Ti_3C_2T_x$ MXene; (iii) explore new possibilities in functionalization technology like the use of the new dopants and surface modifiers to boost selectivity and sensitivity; (iv) uncover hybrid structures and composites based on $Ti_3C_2T_x$ MXene paired with other functional materials, to extract sensing capabilities not available in these material systems alone; (v) design strategies that improve $Ti_3C_2T_x$ MXene sensors' resistance to oxidation, humidity, and other environmental factors which deteriorate sensor performance; (vi) along with that, implement advanced surface treatments or protective coatings to achieve complete operational stability of the $Ti_3C_2T_x$ MXene-based sensors; (vii) extend the application scope of $Ti_3C_2T_x$ MXene-based gas sensors to include biomedical diagnostics, food safety monitoring, and hazardous gas detection in industrial environments; (viii) investigate $Ti_3C_2T_x$ MXene's potential in specialized sensing scenarios, such as detecting biomarkers or volatile organic compounds; and (ix) further, deployment into real-world applications must be seamless and the emphasis should be on compatibility with existing technologies.

By addressing these future directions, the research community can unlock the full potential of $Ti_3C_2T_x$ MXene, paving the way for innovative applications and the widespread adoption of $Ti_3C_2T_x$ MXene-based gas sensors. The continued evolution of this field promises to contribute significantly to developments in sensing technology, environmental monitoring, and public health.

Author Contributions: Conceptualization, R.K.M., A.M.T. and S.M.M.; Investigation, A.M.T., S.M.M. and R.K.M.; Writing—original draft, A.M.T., S.M.M. and R.K.M.; Writing—review & editing, A.M.T., S.M.M., R.K.M., W.J. and J.C.S.; Visualization, A.M.T., R.K.M. and W.J.; Supervision, R.K.M., W.J. and J.C.S.; Project administration, W.J. and J.C.S.; Funding acquisition, J.C.S. All authors have read and agreed to the published version of the manuscript.

Funding: This work was supported by the Technology Innovation Program (RS-2023-00235844, Development of nano-structured materials and devices for super steep sub-threshold swing) funded By the Ministry of Trade, Industry & Energy (MOTIE, Republic of Korea) (1415187621).

Conflicts of Interest: The authors declare no conflict of interest.

References

1. Liu, Y.; Young, S.; Ji, L.; Chu, Y.; Chang, S. High-sensitive ethanol gas sensor using Ag modified ZnO nanosheets. *Talanta Open* **2024**, *10*, 100386. [CrossRef]
2. Sun, G.; Sun, S.; Wang, Y.; Hao, X.; Hao, Y.; Liu, C.; Gong, C.; Yang, Q.; Du, W.; Cheng, P. A novel gas sensor based on ZnO nanoparticles self-assembly porous networks for morphine drug detection in methanol. *Sens. Actuators B* **2024**, *420*, 136495. [CrossRef]
3. Gao, C.; Fu, M.; Fan, S.; Ma, Z.; Tang, Y.; Hou, D.; Cao, Y. High-performance virtual sensors array based on a single-chip FBAR for volatile organic compounds (VOCs) detection and classification. *Sens. Actuators B* **2024**, *422*, 136687. [CrossRef]
4. Tang, Z.; Liu, Y.; Xiang, M.; Cui, D.; Li, Q. Discrimination of VOCs with e-nose consisting of a single MEMS sensor using lightweight deep learning model based on SqueezeNet. *Sens. Actuators B* **2024**, *422*, 136640. [CrossRef]
5. Davis, D.; Narayanan, S.K.; Ajeev, A.; Nair, J.; Jeeji, J.; Vijayan, A.; Kuttyadi, M.V.; Sathian, A.N.; Arulraj, A.K. Flexible paper-based room-temperature acetone sensors with ultrafast regeneration. *ACS Appl. Mater. Interfaces* **2023**, *15*, 25734–25743. [CrossRef]
6. He, X.; Guo, P.; Ren, X.; An, X.; Li, Y.; Liang, S.; Wang, Z.; Zhang, J. High-performance ammonia gas sensor based on a catalytic ruthenium-gated field-effect transistor. *ACS Appl. Nano Mater.* **2024**, *7*, 16395–16403. [CrossRef]
7. Maity, A.; Mitra, S.; Ghosh, B. Textile based lead-free halide perovskite $CH_3NH_3SnI_3$ ammonia gas sensor working at room temperature. *ACS Appl. Electron. Mater.* **2024**, *6*, 2677–2682. [CrossRef]
8. Wu, Y.; Chen, W.; Long, X.; Zhai, R.; Qin, F.; Zhao, Z.; Wang, B.; Zhang, S.; Pan, S. Low temperature ammonia sensor with giant sensitivity and selectivity based on $W@WO_{2.92}$ internal ohmic contact core-shell nanostructures. *Sens. Actuators B* **2025**, *423*, 136792. [CrossRef]
9. Li, H.; Yang, K.; Hu, H.; Qin, C.; Yu, B.; Zhou, S.; Jiang, T.; Ho, D. MXene supported surface plasmon polaritons for optical microfiber ammonia sensing. *Anal. Chem.* **2024**, *96*, 11823–11831. [CrossRef]

10. Li, J.; Hauryliuk, A.; Malings, C.; Eilenberg, S.R.; Subramanian, R.; Presto, A.A. Characterizing the aging of alphasense NO_2 sensors in long-term field deployments. *ACS Sens.* **2021**, *6*, 2952–2959. [CrossRef]
11. Murugesh, P.; Ganesan, M.; Udaiyar, P.S.; Krishnan, H.S.; Jayaram, A.; Mani, N. Mesoporous Co_3O_4/SnO_2 nanostructure-based heterojunctions for NO_2 sensors. *ACS Appl. Nano Mater.* **2023**, *6*, 17433–17444. [CrossRef]
12. Guo, L.; Han, H.; Wang, J.; Wang, P.; Du, C.; Wang, B.; Yuan, Q.; Zhai, Y.; Zhang, C. Defective Cr_2CT_x-based sensors with high sensitivity for NO_2 detection at room temperature. *J. Mater. Chem. A* **2024**, *12*, 20414–20424. [CrossRef]
13. Shao, B.; Liu, Y.; Zhuang, X.; Hou, S.; Han, S.; Yu, X.; Yu, J. Crystallinity and grain boundary control of TIPS-pentacene in organic thin-film transistors for the ultra-high sensitive detection of NO_2. *J. Mater. Chem. C* **2019**, *7*, 10196–10202. [CrossRef]
14. Aravind, A.M.; Tomy, M.; Kuttapan, A.; Aippunny, A.M.K.; Suryabai, X.T. Progress of 2D MXene as an Electrode Architecture for Advanced Supercapacitors: A Comprehensive Review. *ACS Omega* **2023**, *8*, 44375–44394. [CrossRef]
15. Chen, X.; Shi, Z.; Tian, Y.; Lin, P.; Wu, D.; Li, X.; Dong, B.; Xu, W.; Fang, X. Two-dimensional Ti_3C_2 MXene-based nanostructures for emerging optoelectronic applications. *Mater. Horiz.* **2021**, *8*, 2929–2963. [CrossRef]
16. Jin, J.; Xiao, T.; Zhang, Y.-f.; Zheng, H.; Wang, H.; Wang, R.; Gong, Y.; He, B.; Liu, X.; Zhou, K. Hierarchical MXene/transition metal chalcogenide heterostructures for electrochemical energy storage and conversion. *Nanoscale* **2021**, *13*, 19740–19770. [CrossRef]
17. Ayodhya, D. A review of recent progress in 2D MXenes: Synthesis, properties, and applications. *Diamond Relat. Mater.* **2023**, *132*, 109634. [CrossRef]
18. Jyoti, J.; Singh, B.P.; Sandhu, M.; Tripathi, S.K. New insights on MXene and its advanced hybrid materials for lithium-ion batteries. *Sustain. Energy Fuels* **2022**, *6*, 971–1013. [CrossRef]
19. Murali, G.; Modigunta, J.K.R.; Park, Y.H.; Lee, J.-H.; Rawal, J.; Lee, S.-Y.; In, I.; Park, S.-J. A Review on MXene synthesis, stability, and photocatalytic applications. *ACS Nano* **2022**, *16*, 13370–13429. [CrossRef]
20. Ma, R.; Chen, Z.; Zhao, D.; Zhang, X.; Zhuo, J.; Yin, Y.; Wang, X.; Yang, G.; Yi, F. $Ti_3C_2T_x$ MXene for electrode materials of supercapacitors. *J. Mater. Chem. A* **2021**, *9*, 11501–11529. [CrossRef]
21. Hu, G.; Cen, Z.; Xiong, Y.; Liang, K. Progress of high performance $Ti_3C_2T_x$ MXene nanocomposite films for electromagnetic interference shielding. *Nanoscale* **2023**, *15*, 5579–5597. [CrossRef]
22. Nouseen, S.; Ghosh, K.; Pumera, M. Hydrofluoric acid-free etched MAX on 3D-printed nanocarbon electrode for photoelectrochemical hydrogen production. *Appl. Mater. Today* **2024**, *36*, 101995. [CrossRef]
23. Wang, S.; Liu, Y.; Liu, Y.; Hu, W. Effect of HF etching on titanium carbide ($Ti_3C_2T_x$) microstructure and its capacitive properties. *Chem. Eng. J.* **2023**, *452*, 139512. [CrossRef]
24. Wang, C.; Shou, H.; Chen, S.; Wei, S.; Lin, Y.; Zhang, P.; Liu, Z.; Zhu, K.; Guo, X.; Wu, X.; et al. HCl-based hydrothermal etching strategy toward fluoride-free MXenes. *Adv. Mater.* **2021**, *33*, 2101015. [CrossRef]
25. Sun, W.; Shah, S.A.; Chen, Y.; Tan, Z.; Gao, H.; Habib, T.; Radovic, M.; Green, M.J. Electrochemical etching of Ti_2AlC to Ti_2CT_x (MXene) in low-concentration hydrochloric acid solution. *J. Mater. Chem. A* **2017**, *5*, 21663–21668. [CrossRef]
26. Sui, J.; Chen, X.; Li, Y.; Peng, W.; Zhang, F.; Fan, X. MXene derivatives: Synthesis and applications in energy convention and storage. *RSC Adv.* **2021**, *11*, 16065–16082. [CrossRef]
27. Siddique, S.; Waheed, A.; Iftikhar, M.; Mehran, M.T.; Zarif, M.Z.; Arafat, H.A.; Hussain, S.; Shahzad, F. Fluorine-free MXenes via molten salt Lewis acidic etching: Applications, challenges, and future outlook. *Prog. Mater Sci.* **2023**, *139*, 101183. [CrossRef]
28. Doan, T.H.P.; Hong, W.G.; Noh, J.-S. Palladium nanoparticle-decorated multi-layer $Ti_3C_2T_x$ dual-functioning as a highly sensitive hydrogen gas sensor and hydrogen storage. *RSC Adv.* **2021**, *11*, 7492–7501. [CrossRef]
29. Sun, B.; Lv, H.; Liu, Z.; Wang, J.; Bai, X.; Zhang, Y.; Chen, J.; Kan, K.; Shi, K. Co_3O_4@PEI/$Ti_3C_2T_x$ MXene nanocomposites for a highly sensitive NO_x gas sensor with a low detection limit. *J. Mater. Chem. A* **2021**, *9*, 6335–6344. [CrossRef]
30. Fan, C.; Shi, J.; Zhang, Y.; Quan, W.; Chen, X.; Yang, J.; Zeng, M.; Zhou, Z.; Su, Y.; Wei, H.; et al. Fast and recoverable NO_2 detection achieved by assembling ZnO on $Ti_3C_2T_x$ MXene nanosheets under UV illumination at room temperature. *Nanoscale* **2022**, *14*, 3441–3451. [CrossRef]
31. Chen, J.; Qin, W.; Li, K.; Feng, L.; Chen, J.; Qiao, H.; Yang, M.; Tian, Z.; Li, X.; Gu, C.; et al. A high-sensitivity, fast-response and high-stability humidity sensor of curly flake $Ti_3C_2T_x$ MXene prepared by electrolytic intercalation of NaOH solution. *J. Mater. Chem. A* **2022**, *10*, 22278–22288. [CrossRef]
32. Fan, J.; Gao, J.; Lv, H.; Jiang, L.; Qin, F.; Fan, Y.; Sun, B.; Wang, J.; Ikram, M.; Shi, K. Synthesis and characterization of an ultra-thin BiOCl/MXene heterostructure for the detection of NO_2 at room temperature with enhanced moisture resistance. *J. Mater. Chem. A* **2022**, *10*, 25714–25724. [CrossRef]
33. Yu, Q.; Pan, J.; Li, J.; Su, C.; Huang, Y.; Bi, S.; Jiang, J.; Chen, N. A general strategy to immobilize metal nanoparticles on MXene composite fabrics for enhanced sensing performance and endowed multifunctionality. *J. Mater. Chem. C* **2022**, *10*, 13143–13156. [CrossRef]
34. Lim, G.P.; Soon, C.F.; Morsin, M.; Ahmad, M.K.; Nayan, N.; Tee, K.S. Synthesis, characterization and antifungal property of $Ti_3C_2T_x$ MXene nanosheets. *Ceram. Int.* **2020**, *46*, 20306–20312. [CrossRef]

35. Kim, S.; Byun, S.; Yuk, S.; Choi, S.; Song, S.H.; Lee, D. Dimensionally integrated hybrid films of $Ti_3C_2T_x$ MXene and cellulose nanocrystals for high-performance supercapacitors. *J. Mater. Res. Technol.* **2024**, *33*, 9268–9275. [CrossRef]
36. Aïssa, B.; Ali, A.; Mahmoud, K.A.; Haddad, T.; Nedil, M. Transport properties of a highly conductive 2D $Ti_3C_2T_x$ MXene/graphene composite. *Appl. Phys. Lett.* **2016**, *109*, 043109. [CrossRef]
37. Yao, L.; Tian, X.; Cui, X.; Zhao, R.; Xiao, X.; Wang, Y. Partially oxidized $Ti_3C_2T_x$ MXene-sensitive material-based ammonia gas sensor with high-sensing performances for room temperature application. *J. Mater. Sci. Mater. Electron.* **2021**, *32*, 27837–27848. [CrossRef]
38. Huang, J.H.R.; Tseng, S.-W.; Chen, I.-W.P. In-situ electrochemical XRD and raman probing of ion transport dynamics in ionic liquid-etched $Ti_3C_2T_x$ MXene for energy storage applications. *Chem. Eng. J.* **2024**, *503*, 158232. [CrossRef]
39. Zachariah, S.; Indirajith, R.; Rajalakshmi, M. Recent advances in optoelectronic properties and applications of $Ti_3C_2T_x$ MXene. *J. Alloys Compd.* **2025**, *1011*, 178296. [CrossRef]
40. Verma, K.D.; Kar, K.K. Cost-effective synthesis route for ultra-high purity of Ti_3AlC_2 MAX phase with enhanced performance of $Ti_3C_2T_x$ MXene and MXene/NiO composite for supercapacitor application. *Chem. Eng. J.* **2025**, *504*, 158938. [CrossRef]
41. Khan, U.; Irshad, A.; Kong, L.B.; Que, W. Synthesis of fluorine-free $Ti_3C_2T_x$ MXenes via acidic activation for enhanced electrochemical applications. *J. Alloys Compd.* **2025**, *1010*, 177097. [CrossRef]
42. Bai, X.; Guo, Y.; Yan, H.; Liu, J.; Li, J.; Lu, H. Achieving excellent microwave absorption performance in ultralight $Ti_3C_2T_x$ MXene with M-O bonds (M = Fe, Co, Ni) as surface terminating groups. *Chem. Eng. J.* **2024**, *501*, 157715. [CrossRef]
43. Niu, X.; Lu, X.; He, B.; Xiao, X.; Wang, S.; Liang, Z.; Shi, Q.; Ma, L.-F. Dual electron transfer path and $Ti_3C_2T_x$ LSPR photothermal enhancement in 2D/2D/2D $Ti_3C_2T_x$ MXene@TiO_2/$CdIn_2S_4$ ternary heterojunction for enhanced photocatalytic H_2 production: Construction, kinetics, and mechanistic insights. *Appl. Catal. B* **2025**, *361*, 124703. [CrossRef]
44. Cui, J.; Wu, J.; Feng, A.; Yu, Y.; Mi, L.; Yu, Y. Low infrared emissivity and oxidation stability of $Ti_3C_2T_x$ MXene-based composite with tannic acid. *Chem. Eng. J.* **2024**, *493*, 152289. [CrossRef]
45. Lian, Y.; Lan, D.; Jiang, X.; Wang, L.; Yan, S.; Dong, Q.; Jiang, Y.; Gu, J.; Gao, Z.; Wu, G. Multifunctional electromagnetic wave absorbing carbon fiber/$Ti_3C_2T_X$ MXene fabric with superior near-infrared laser dependent photothermal antibacterial behaviors. *J. Colloid Interface Sci.* **2024**, *676*, 217–226. [CrossRef]
46. Jiang, G.; Ye, G.; Feng, Z.; Qi, L.; Wang, C.; Xing, W.; Gui, Z.; Song, L.; Hu, Y. Linear polydichlorophosphazene and $Ti_3C_2T_x$ MXene nanohybrids: Synthesis and application to epoxy resin to improve the fire safety and mechanical properties. *J. Colloid Interface Sci.* **2025**, *679*, 141–151. [CrossRef]
47. Iqbal, A.; Hamdan, N.M. Investigation and optimization of mxene functionalized mesoporous titania films as efficient photoelectrodes. *Materials* **2020**, *14*, 6292. [CrossRef]
48. Xu, J.; Pi, X.; Qi, K.; Zhang, S.; Wang, Y.; Man, Z.; Yang, C.; Tang, Q.; An, C.; Zhang, Y.; et al. Chitosan derived nitrogen and oxygen dual-doped hierarchical porous carbon/$Ti_3C_2T_x$ MXene fiber for flexible cable shaped lithium-selenium battery. *Int. J. Biol. Macromol.* **2024**, *282*, 136836. [CrossRef]
49. Shahzad, A.; Rasool, K.; Miran, W.; Nawaz, M.; Jang, J.; Mahmoud, K.A.; Lee, D.S. Two-dimensional $Ti_3C_2T_x$ MXene nanosheets for efficient copper removal from water. *ACS Sustain. Chem. Eng.* **2017**, *5*, 11481–11488. [CrossRef]
50. Eom, W.; Shin, H.; Han, T.H. Tracking the thermal dynamics of $Ti_3C_2T_x$ MXene with XPS and two-dimensional correlation spectroscopy. *Appl. Phys. Lett.* **2023**, *122*, 211601. [CrossRef]
51. Wen, Y.; Rufford, T.E.; Chen, X.; Li, N.; Lyu, M.; Dai, L.; Wang, L. Nitrogen-doped $Ti_3C_2T_x$ MXene electrodes for high-performance supercapacitors. *Nano Energy* **2017**, *38*, 368–376. [CrossRef]
52. Näslund, L.; Kokkonen, E.; Magnuson, M. Interaction and kinetics of H_2, CO_2, and H_2O on $Ti_3C_2T_x$ MXene probed by X-ray photoelectron spectroscopy. *Appl. Surf. Sci.* **2025**, *684*, 161926. [CrossRef]
53. Sunderiya, S.; Suragtkhuu, S.; Purevdorj, S.; Ochirkhuyag, T.; Bat-Erdene, M.; Myagmarsereejid, P.; Slattery, A.D.; Bati, A.S.R.; Shapter, J.G.; Odkhuu, D.; et al. Understanding the oxidation chemistry of $Ti_3C_2T_x$ (MXene) sheets and their catalytic performances. *J. Energy Chem.* **2023**, *88*, 437–445. [CrossRef]
54. Jiang, Y.; Sun, T.; Xie, X.; Jiang, W.; Li, J.; Tian, B.; Su, C. Oxygen-functionalized ultrathin $Ti_3C_2T_x$ MXene for enhanced electrocatalytic hydrogen evolution. *ChemSusChem* **2019**, *12*, 1368–1373. [CrossRef]
55. Wang, J.; Cai, Z.; Lin, D.; Chen, K.; Zhao, L.; Xie, F.; Su, R.; Xie, W.; Liu, P.; Zhu, R. Plasma oxidized $Ti_3C_2T_x$ mxene as electron transport layer for efficient perovskite solar cells. ACS Appl. *Mater. Interfaces* **2021**, *13*, 32495–33250. [CrossRef]
56. Hu, Z.; Xie, Y.; Yu, D.; Liu, Q.; Zhou, L.; Zhang, K.; Li, P.; Hu, F.; Li, L.; Chou, S.; et al. Hierarchical $Ti_3C_2T_x$ MXene/carbon nanotubes for low overpotential and long-life Li-CO_2 Batteries. *ACS Nano* **2021**, *15*, 8407–8417. [CrossRef]
57. Wang, F.; Yang, C.H.; Duan, C.Y.; Xiao, D.; Tang, Y.; Zhu, J.F. An organ-like titanium carbide material (MXene) with multilayer structure encapsulating hemoglobin for a mediator-free biosensor. *J. Electrochem. Soc.* **2015**, *162*, B16–B21. [CrossRef]
58. Wang, H.; Zheng, R.; Shu, C.; Long, J. Promoting the electrocatalytic activity of $Ti_3C_2T_x$ MXene by modulating CO_2 adsorption through oxygen vacancies for high-performance lithium-carbon dioxide batteries. *ChemElectroChem* **2020**, *7*, 4922–4930. [CrossRef]

59. Zhang, R.; Xue, Y.; Ma, M.; Han, Y.; Tian, J. Cu-Bi bimetallic sulfides loaded on two-dimensional $Ti_3C_2T_x$ MXene for efficient electrocatalytic nitrogen reduction under ambient conditions. *Nano Lett.* **2024**, *24*, 10297–10304. [CrossRef]
60. Ghosh, K.; Giri, P. Experimental and theoretical study on the role of 2D $Ti_3C_2T_x$ MXenes on superior charge transport and ultra-broadband photodetection in MXene/Bi_2S_3 nanorod composite through local Schottky junctions. *Carbon* **2024**, *216*, 118515. [CrossRef]
61. Ma, W.; Chen, H.; Hou, S.; Huang, Z.; Huang, Y.; Xu, S.; Fan, F.; Chen, Y. Compressible highly stable 3D porous MXene/GO foam with a tunable high-performance stealth property in the terahertz band. *ACS Appl. Mater. Interfaces* **2019**, *11*, 25369–25377. [CrossRef] [PubMed]
62. Wu, Z.; Shen, J.; Li, Z.; Liu, S.; Zhou, Y.; Feng, K.; Zhang, B.; Zhao, S.; Xue, D.; He, J.; et al. Anisotropic plasmon resonance in $Ti_3C_2T_x$ MXene enables site-selective plasmonic catalysis. *ACS Nano* **2025**, *19*, 1832–1844. [CrossRef] [PubMed]
63. Hantanasirisakul, K.; Zhao, Q.; Urbankowski, P.; Halim, J.; Anasori, B.; Kota, S.; Ren, C.E.; Barsoum, M.W.; Gogotsi, Y. Fabrication of $Ti_3C_2T_x$ MXene transparent thin films with tunable optoelectronic properties. *Adv. Electron. Mater.* **2016**, *2*, 1600050. [CrossRef]
64. Li, Y.; Xiong, C.; Huang, H.; Peng, X.; Mei, D.; Li, M.; Liu, G.; Wu, M.; Zhao, T.; Huang, B. 2D $Ti_3C_2T_x$ MXenes: Visible black but infrared white materials. *Adv. Mater.* **2021**, *33*, 2103054. [CrossRef]
65. Cao, W.; Nie, J.; Cao, Y.; Gao, C.; Wang, M.; Wang, W.; Lu, X.; Ma, X.; Zhong, P. A review of how to improve $Ti_3C_2T_x$ MXene stability. *Chem. Eng. J.* **2024**, *496*, 154097. [CrossRef]
66. Zheng, H.; Chen, J.; Que, M.; Liu, X.; Yang, L.; Zhao, Y.; Li, Y.; Yang, X.; Yang, T.; Liu, Z. Light absorption and photocatalytic activity enhanced by in situ formation of uniform TiO_2 nanoparticles on two-dimensional $Ti_3C_2T_x$ surface. *J. Alloys Compd.* **2021**, *882*, 160757. [CrossRef]
67. Limbu, T.B.; Chitara, B.; Cervantes, M.Y.G.; Zhou, Y.; Huang, S.; Tang, Y.; Yan, F. Unravelling the thickness dependence and mechanism of surface-enhanced raman scattering on $Ti_3C_2T_X$ MXene nanosheets. *Phys. Chem. C* **2020**, *124*, 17772–17782. [CrossRef]
68. Elumalai, S.; Yoshimura, M.; Ogawa, M. Simultaneous delamination and rutile formation on the surface of $Ti_3C_2T_x$ MXene for copper adsorption. *Chem. Asian J.* **2020**, *15*, 1044–1051. [CrossRef]
69. Jiang, W.; Lee, S.; Zhao, K.; Lee, K.; Han, H.; Oh, J.; Lee, H.; Kim, H.; Koo, C.M.; Park, C. Flexible and transparent electrode of hybrid Ti3C2TX MXene–silver nanowires for high-performance quantum dot light-emitting diodes. *ACS Nano* **2022**, *16*, 9203–9213. [CrossRef]
70. Xu, G.; Niu, Y.; Yang, X.; Jin, Z.; Wang, Y.; Xu, Y.; Niu, H. Preparation of $Ti_3C_2T_x$ MXene-derived quantum dots with white/blue-emitting photoluminescence and electrochemiluminescence. *Adv. Opt. Mater.* **2018**, *6*, 1800951. [CrossRef]
71. Li, J.; Li, Y.; Zhang, F.; Tang, Z.; Xu, Y. Visible-light-driven integrated organic synthesis and hydrogen evolution over 1D/2D CdS-$Ti_3C_2T_x$ MXene composites. *Appl. Catal. B* **2020**, *269*, 118783. [CrossRef]
72. Han, W.; Wen, X.; Ding, Y.; Li, Z.; Lu, M.; Zhu, H.; Wang, G.; Yan, J.; Hong, X. Ultraviolet emissive $Ti_3C_2T_x$ MXene quantum dots for multiple anti-counterfeiting. *Appl. Surf. Sci.* **2022**, *595*, 153563. [CrossRef]
73. Hou, T.; Li, Q.; Zhang, Y.; Zhu, W.; Yu, K.; Wang, S.; Xu, Q.; Liang, S.; Wang, L. Near-infrared light-driven photofixation of nitrogen over Ti3C2Tx/TiO2 hybrid structures with superior activity and stability. *Appl. Catal. B* **2020**, *273*, 119072. [CrossRef]
74. Xie, X.; Zhang, N.; Tang, Z.; Anpo, M.; Xu, Y. $Ti_3C_2T_x$ MXene as a Janus cocatalyst for concurrent promoted photoactivity and inhibited photocorrosion. *Appl. Catal. B* **2018**, *237*, 43–49. [CrossRef]
75. Li, H.; Fan, R.; Zou, B.; Yan, J.; Shi, Q.; Guo, G. Roles of MXenes in biomedical applications: Recent developments and prospects. *J. Nanobiotechnol.* **2023**, *21*, 73. [CrossRef]
76. Jun, B.; Heo, J.; Taheri-Qazvini, N.; Park, C.M.; Yoon, Y. Adsorption of selected dyes on $Ti_3C_2T_x$ MXene and Al-based metal-organic framework. *Ceram. Int.* **2020**, *46*, 2960–2968. [CrossRef]
77. Wang, L.; Chen, L.; Song, P.; Liang, C.; Lu, Y.; Qiu, H.; Zhang, Y.; Kong, J.; Gu, J. Fabrication on the annealed $Ti_3C_2T_x$ MXene/Epoxy nanocomposites for electromagnetic interference shielding application. *Compos. Part B* **2019**, *171*, 111–118. [CrossRef]
78. Karthikeyan, P.; Elanchezhiyan, S.; Preethi, J.; Talukdar, K.; Meenakshi, S.; Park, C.M. Two-dimensional (2D) $Ti_3C_2T_x$ MXene nanosheets with superior adsorption behavior for phosphate and nitrate ions from the aqueous environment. *Ceram. Int.* **2020**, *47*, 732–739. [CrossRef]
79. Pan, Y.; Fu, L.; Zhou, Q.; Wen, Z.; Lin, T.; Yu, J.; Wang, W.; Zhao, H. Flammability, thermal stability and mechanical properties of polyvinyl alcohol nanocomposites reinforced with delaminated $Ti_3C_2T_x$ (MXene). *Polym. Compos.* **2019**, *41*, 210–218. [CrossRef]
80. Mayerberger, E.A.; Urbanek, O.; McDaniel, R.M.; Street, R.M.; Barsoum, M.W.; Schauer, C.L. Preparation and characterization of polymer-$Ti_3C_2T_x$ (MXene) composite nanofibers produced via electrospinning. *J. Appl. Polym. Sci.* **2017**, *134*, 45295. [CrossRef]
81. Li, S.; Huang, H.; Chen, F.; He, X.; Ma, Y.; Zhang, L.; Sheng, X.; Chen, Y.; Shchukina, E.; Shchukin, D. Reinforced anticorrosion performance of waterborne epoxy coating with eco-friendly L-cysteine modified $Ti_3C_2T_x$ MXene nanosheets. *Prog. Org. Coat.* **2021**, *161*, 106478. [CrossRef]
82. Wang, T.; Sun, X.; Guo, X.; Zhang, J.; Yang, J.; Tao, S.; Guan, J.; Zhou, L.; Han, J.; Wang, C.; et al. Ultraefficiently calming cytokine storm using $Ti_3C_2T_x$ MXene. *Small Methods* **2021**, *5*, 2001108. [CrossRef] [PubMed]

83. Kumar, G.; Ahlawat, A.; Bhardwaj, H.; Sahu, G.K.; Rana, P.S.; Solanki, P.R. Ultrasonication-assisted synthesis of transition metal carbide of MXene: An efficient and promising material for photocatalytic organic dyes degradation of rhodamine B and methylene blue in wastewater. *Environ. Sci. Pollut. Res.* **2024**, *31*, 38232–38250. [CrossRef]
84. Zhang, L.; Su, W.; Shu, H.; Lü, T.; Fu, L.; Song, K.; Huang, X.; Yu, J.; Lin, C.; Tang, Y. Tuning the photoluminescence of large $Ti_3C_2T_x$ MXene flakes. *Ceram. Int.* **2019**, *45*, 11468–11474. [CrossRef]
85. Elumalai, S.; Lombardi, J.R.; Yoshimura, M. The surface-enhanced resonance Raman scattering of dye molecules adsorbed on two-dimensional titanium carbide $Ti_3C_2T_x$ (MXene) film. *Mater. Adv.* **2020**, *1*, 146–152. [CrossRef]
86. Du, Y.; Zhang, X.; Wei, L.; Yu, B.; Ma, D.; Ye, S. Electrodeposition of a Ni-P-TiO_2/$Ti_3C_2T_x$ coating with in situ grown nanoparticles TiO_2 on $Ti_3C_2T_x$ Sheets. *Coatings* **2019**, *9*, 750. [CrossRef]
87. Sarmah, H.S.; Ghosh, S. Surface passivation and tunable magnetic properties of Cr-based MXenes. *J. Phys. Chem. C* **2024**, *128*, 16133–16142. [CrossRef]
88. Wang, S.; Liu, Y.; Liu, Y.; Shi, Z.; Zhou, J.; Zhu, J.; Hu, W. Identifying the surface properties of $Ti_3C_2T_x$ MXene through transmission electron microscopy. *Cell Rep. Phys. Sci.* **2022**, *3*, 101151. [CrossRef]
89. Schied, M.; Pazniak, H.; Brette, F.; Lacovig, P.; Paris, M.; Boucher, F.; Lizzit, S.; Mauchamp, V.; Larciprete, R. Reactivity of $Ti_3C_2T_x$ MXene with atomic hydrogen: Tuning of surface terminations by halogen removal and reversible O to OH conversion. *Chem. Mater.* **2024**, *36*, 11905–11919. [CrossRef]
90. Bae, S.; Kang, Y.; Khazaei, M.; Ohno, K.; Kim, Y.; Han, M.; Chang, K.; Raebiger, H. Electronic and magnetic properties of carbide MXenes-The role of electron correlations. *Mater. Today Adv.* **2021**, *9*, 100118. [CrossRef]
91. Ronchi, R.M.; Santos, S.F.; Veiga, R.G. Interfacial properties of polyethylene/$Ti_3C_2T_x$ mxene nanocomposites investigated by first-principles calculations. *Appl. Surf. Sci.* **2023**, *609*, 155344. [CrossRef]
92. Rostami, M.; Rezvaninia, P.; Amiri, A.; Ziarani, G.M.; Ganjali, M.R.; Badiei, A. Hybrid nano-architectural engineering of $Ti_3C_2T_x$ MXene heterostructures for supercapacitor applications: A review. *Results Eng.* **2024**, *22*, 102227. [CrossRef]
93. Kim, S.J.; Koh, H.-J.; Ren, C.E.; Kwon, O.; Maleski, K.; Cho, S.-Y.; Anasori, B.; Kim, C.-K.; Choi, Y.-K.; Kim, J.; et al. Metallic $Ti_3C_2T_x$ MXene gas sensors with ultrahigh signal-to-noise ratio. *ACS Nano* **2018**, *12*, 986–993. [CrossRef] [PubMed]
94. Montazeri, M.; Masoudpanah, S.; Sarkar, T.; Aslibeiki, B. Enhancement of microwave absorption performance of cobalt ferrite by adding MXene ($Ti_3C_2T_x$) nanosheets. *Mater. Chem. Phys.* **2024**, *322*, 129608. [CrossRef]
95. G.-Romeral, N.; Morales-García, Á.; Viñes, F.; Moreira, I.d.P.R.; Illas, F. Theoretical analysis of magnetic coupling in the Ti_2C bare MXene. *J. Phys. Chem. C* **2023**, *127*, 3706–3714. [CrossRef] [PubMed]
96. Da Rocha, J.D.G.; Cechinel, M.A.P.; Rocha, L.F.; Riella, H.G.; Padoin, N.; Soares, C. Exploring the potential of rare earth doped carbon dots: Concepts and applications. *Chem. Eng. J. Adv.* **2024**, *17*, 100583. [CrossRef]
97. Yang, Y.; Anayee, M.; Pattammattel, A.; Shekhirev, M.; Wang, R.; Huang, X.; Chu, Y.S.; Gogotsi, Y.; May, S.J. Enhanced magnetic susceptibility in $Ti_3C_2T_x$ MXene with Co and Ni incorporation. *Nanoscale* **2024**, *16*, 5760–5767. [CrossRef]
98. Rafiq, S.; Awan, S.; Zheng, R.; Wen, Z.; Rani, M.; Akinwande, D.; Rizwan, S. Novel room-temperature ferromagnetism in Gd-doped 2-dimensional $Ti_3C_2T_x$ MXene semiconductor for spintronics. *J. Magn. Magn. Mater.* **2020**, *497*, 165954. [CrossRef]
99. Wu, N.; Zhao, W.; Zhou, B.; Wu, Y.; Hou, W.; Xu, W.; Du, J.; Zhong, W. 3D nitrogen-doped $Ti_3C_2T_x$/rGO foam with marco- and microporous structures for enhance supercapacitive performance. *Electrochim. Acta* **2022**, *404*, 139752. [CrossRef]
100. Bhat, A.; Anwer, S.; Bhat, K.S.; Mohideen, M.I.; Liao, K.; Qurashi, A. Prospects challenges and stability of 2D MXenes for clean energy conversion and storage applications. *NJP 2D Mater. Appl.* **2021**, *5*, 61. [CrossRef]
101. Kewate, O.J.; Punniyakoti, S. Ti_3AlC_2 MAX phase and $Ti_3C_2T_X$ MXene-based composites towards supercapacitor applications: A comprehensive review of synthesis, recent progress, and challenges. *J. Energy Storage* **2023**, *72*, 108501. [CrossRef]
102. Zhang, K.; Di, M.; Fu, L.; Deng, Y.; Du, Y.; Tang, N. Enhancing the magnetism of 2D carbide MXene $Ti_3C_2T_x$ by H_2 annealing. *Carbon* **2020**, *157*, 90–96. [CrossRef]
103. Zhang, X.; Wang, H.; Hu, R.; Huang, C.; Zhong, W.; Pan, L.; Feng, Y.; Qiu, T.; Zhang, C.; Yang, J. Novel solvothermal preparation and enhanced microwave absorption properties of $Ti_3C_2T_x$ MXene modified by in situ coated Fe_3O_4 nanoparticles. *Appl. Surf. Sci.* **2019**, *484*, 383–391. [CrossRef]
104. Matias, M.L.; Pereira, C.; Almeida, H.V.; Jana, S.; Panigrahi, S.; Menda, U.D.; Nunes, D.; Fortunato, E.; Martins, R.; Nandy, S. 3D printed MXene architectures for a plethora of smart applications. *Mater. Today Adv.* **2024**, *23*, 100512. [CrossRef]
105. Liu, X.; Ma, J.; Zhang, S.; Guan, G.; Yang, Q.; Wang, J. $Ti_3C_2T_x$ MXene coupled with CdS for enhanced photocatalytic H_2 production. *Int. J. Hydrogen Energy* **2025**, *101*, 1191–1200. [CrossRef]
106. Aydin, E.; E.-Demellawi, J.K.; Yarali, E.; Aljamaan, F.; Sansoni, S.; Rehman, A.u.; Harrison, G.; Kang, J.; Labban, A.E.; Bastiani, M.D.; et al. Scaled deposition of $Ti_3C_2T_x$ MXene on complex surfaces: Application assessment as rear electrodes for silicon heterojunction solar cells. *ACS Nano* **2022**, *16*, 2419–2428. [CrossRef]
107. Mozafari, M.; Soroush, M. Surface functionalization of MXenes. *Mater. Adv.* **2021**, *2*, 7277–7307. [CrossRef]
108. Deen, M.A.; Rajendran, H.K.; Chandrasekar, R.; Ghosh, D.; Narayanasamy, S. The Rise of $Ti_3C_2T_x$ MXene synthesis strategies over the decades: A review. *FlatChem* **2024**, *47*, 100734. [CrossRef]

109. K T, M.S.; Karupppanan, P. A review of the revolutionary impact of MXene marvel in perovskite solar cells. *Chem. Phys. Impact* **2024**, *8*, 100610. [CrossRef]
110. Bilibana, M.P. Electrochemical properties of MXenes and applications. *Adv. Sens. Energy Mater.* **2023**, *2*, 100080. [CrossRef]
111. Zhang, J.; Yang, X.; Chen, C.; Li, Y.; Li, J.; Chen, W.; Cui, Y.; Li, X.; Zhu, X. Surface phosphorus grafting of $Ti_3C_2T_x$ MXene as an interface charge "bridge" for efficient electrocatalytic hydrogen evolution in all-ph media. *Chem. Mater.* **2024**, *36*, 12006–12017. [CrossRef]
112. Cheng, R.; Hu, T.; Yang, J.; Wang, Z.; Wang, W.; Liang, Y.; Yang, Z.; Zhang, H.; Wang, X. Nitrogen and sulfur co-doped $Ti_3C_2T_x$ MXenes for high-rate lithium-ion batteries. *Phys. Chem. Chem. Phys.* **2023**, *25*, 10635–10646. [CrossRef] [PubMed]
113. Anasori, B.; Shi, C.; Moon, E.J.; Xie, Y.; Voigt, C.A.; Kent, P.R.C.; May, S.J.; Billinge, S.J.L.; Barsouma, M.W.Y. Gogotsi, Control of electronic properties of 2D carbides (MXenes) by manipulating their transition metal layers. *Nanoscale Horiz.* **2016**, *1*, 227–234. [CrossRef] [PubMed]
114. Chu, Y.Z.; Lau, K.C. A first-principles study of multilayer $Ti_3C_2T_x$ MXene model. *Nanoscale* **2024**, *16*, 19374–19384. [CrossRef]
115. Atkare, S.; Kaushik, S.D.; Jagtap, S.; Rout, C.S. Room-temperature chemiresistive ammonia sensors based on 2D MXenes and their hybrids: Recent developments and future prospects. *Dalton Trans.* **2023**, *52*, 13831–13851. [CrossRef]
116. Radhakrishnan, S.; Rout, C.S. Recent developments in 2D MXene-based materials for next generation room temperature NO_2 gas sensors. *Nanoscale Adv.* **2023**, *5*, 4649–4669. [CrossRef]
117. Zhang, J.; Li, Z.; Yang, H.; Chen, W.; Wang, Z.; Zhou, H.; Li, P.; Sun, X. Application of MXene composites for target gas detection in food safety. *Food Chem.* **2024**, *460*, 140620. [CrossRef]
118. Ta, Q.T.H.; Thakur, D.; Noh, J. Design of functional $Ti_3C_2T_x$ MXene for gas sensors and energy harvesting: A review. *Chemosensors* **2023**, *11*, 477. [CrossRef]
119. Yi, Y.; Li, J.; Bi, X.; Zhang, L.; Ren, Y.; Li, L.; You, T. Highly active $Ti_3C_2T_x$ MXene nanoribbons@AuPt bimetallic nanozyme constructed in a "two birds with one stone" manner for colorimetric sensing of dipterex. *Talanta* **2024**, *281*, 126881. [CrossRef]
120. Jia, J.; Deng, W.; Zhang, H.; Yan, X.; Ma, K.; Zhou, C.; Cao, H.; Jia, X.; Liu, S. MXene ($Ti_3C_2T_x$)/Rh-doped SnO_2 composites for improved acetone sensing properties. *Ceram. Int.* **2024**, *50*, 38970–38980. [CrossRef]
121. Nam, M.S.; Kim, J.; Mirzaei, A.; Kim, H.W.; Kim, S.S. Pd-functionalized $Ti_3C_2T_x$ MXenes for realization of flexible, selective, self-heated H_2 sensing. *Sens. Actuators B* **2024**, *404*, 135189. [CrossRef]
122. Zhu, Z.; Liu, C.; Jiang, F.; Liu, J.; Ma, X.; Liu, P.; Xu, J.; Wang, L.; Huang, R. Flexible and lightweight $Ti_3C_2T_x$ MXene@Pd colloidal nanoclusters paper film as novel H_2 sensor. *J. Hazard. Mater.* **2020**, *399*, 123054. [CrossRef] [PubMed]
123. Qiu, C.; Zhang, H.; Li, Q.; Song, Y.; An, F.; Wang, H.; Wang, S.; Zhu, L.; Lv, C.; Zhang, D. Controllable synthesis of 3D PdCu/$Ti_3C_2T_x$ hierarchical nanostructures for chemiresistive room temperature H_2 sensors. *Sens. Actuators B* **2024**, *417*, 136215. [CrossRef]
124. Yang, Z.; Dong, L.; Chen, Q.; Wang, Z.; Cao, J.; Dong, M.; Wang, J.; Zhang, J.; Huang, X. A comparative study of H_2 sensing performance of stoichiometric polymorphs of titanium carbide MXenes loaded with Pd nanodots. *Phys. Chem. Chem. Phys.* **2023**, *25*, 16438–16445. [CrossRef]
125. Li, B.; Liu, J.; Lin, Z.; Mai, C.; Cao, A.; Yao, D.; Chen, Z.; Qu, F. A fuel cell type gas sensor based on Pt/$Ti_3C_2T_x$ MXene for highly selective detection of NH_3. *Mater. Lett.* **2025**, *383*, 137979. [CrossRef]
126. Zhu, X.; Li, J.; Chang, X.; Gao, W.; Chen, X.; Niu, S.; Sun, S. Room temperature gas sensors for NH_3 detection based on SnO_2 films and lamellar-structured $Ti_3C_2T_x$ MXene heterojunction nanocomposites. *Appl. Surf. Sci.* **2024**, *660*, 159976. [CrossRef]
127. Han, D.; Liu, Z.; Liu, L.; Li, D.; Chen, Y.; Wang, H.; Zhao, L.; Wang, W.; Sang, S. Room temperature and anti-humidity NH3 detection based on GaN nanorods/$Ti_3C_2T_x$ MXene composite gas sensor. *Sens. Actuators B* **2023**, *393*, 134319. [CrossRef]
128. Maina, E.O.; Ni, P.; Dembélé, K.; Dragoe, D.; Yassar, A.; Bouanis, F.Z. Self-assembled $Ti_3C_2T_X$ MXene thin films for high-performance ammonia sensors. *Appl. Surf. Sci.* **2024**, *672*, 160864. [CrossRef]
129. Liu, M.; Ji, J.; Song, P.; Wang, J.; Wang, Q. Sensing performance of α-Fe2O3/$Ti_3C_2T_x$ MXene nanocomposites to NH3 at room temperature. *J. Alloys Compd.* **2022**, *898*, 162812. [CrossRef]
130. Ranjith, K.S.; Sonwal, S.; Mohammadi, A.; Raju, G.S.R.; Huh, Y.S.; Han, Y.-K. Engineering a surface functionalized Pt@SnS_2/$Ti_3C_2T_x$ MXene sensor with humidity tolerance and high sensitivity at room temperature for NH3 detection. *J. Mater. Chem. A* **2025**, *13*, 2950–2964. [CrossRef]
131. Bhardwaj, R.; Hazra, A. SrTiO3 passivated MXene ($Ti_3C_2T_x$) for efficient VOC detection in hazardous humid ambient. *Sens. Actuators B* **2024**, *401*, 134967. [CrossRef]
132. Tian, R.; Wang, Q.; Song, P. Ethanol recognition based on carbon quantum dots sensitized $Ti_3C_2T_x$ MXene and its enhancement effect of ultraviolet condition under low temperature. *Vacuum* **2024**, *230*, 113730. [CrossRef]
133. Song, X.; Liu, T.; Gu, K.; Luo, Z.; Yang, X.; Zhang, M. UV-triggered and temperature-control carrier transport regulation of ZnO/$Ti_3C_2T_x$ MXene heterostructures for dual selective HCHO and triethylamine detection. *Sens. Actuators B* **2024**, *417*, 136158. [CrossRef]

134. Song, X.; Liu, T.; Gu, K.; Luo, Z.; Zhang, M. Highly selective and ultra-sensitive gas sensor based on $Fe_2O_3/Ti_3C_2T_x$ MXene heterostructure for ppb-level n-butanol detection. *J. Alloys Compd.* **2024**, *976*, 173153. [CrossRef]
135. Yao, Y.; Han, Y.; Zhou, M.; Xie, L.; Zhao, X.; Wang, Z.; Barsan, N.; Zhu, Z. $MoO_3/TiO_2/Ti_3C_2T_x$ nanocomposite based gas sensors for highly sensitive and selective isopropanol detection at room temperature. *J. Mater. Chem. A* **2022**, *10*, 8283–8292. [CrossRef]
136. Guo, F.; Feng, C.; Zhang, Z.; Zhang, L.; Xu, C.; Zhang, C.; Lin, S.; Wu, H.; Zhang, B.; Tabusi, A.; et al. A room-temperature NO2 sensor based on Ti3C2TX MXene modified with sphere-like CuO. *Sens. Actuators B* **2023**, *375*, 132885. [CrossRef]
137. Shin, K.Y.; Mirzaei, A.; Oum, W.; Kim, E.B.; Kim, H.M.; Moon, S.; Kim, S.S.; Kim, H.W. Enhanced NO_2 gas response of ZnO-$Ti_3C_2T_x$ MXene nanocomposites by microwave irradiation. *Sens. Actuators B* **2024**, *409*, 135605. [CrossRef]
138. Tang, L.; Yang, H.; Wang, H.; Yang, Y.; Wang, X.; Tang, G.; Zeng, D. Molten salt-modified $Ti_3C_2T_x$ MXene with tunable oxygen-functionalized surfaces for effective detection of NO_2 at room temperature. *Ceram. Int.* **2024**, *50*, 21619–21629. [CrossRef]
139. Hu, J.; Wang, X.; Lei, H.; Luo, M.; Zhang, Y. Plasmonic photothermal driven MXene-based gas sensor for highly sensitive NO_2 detection at room temperature. *Sens. Actuators B* **2024**, *407*, 135422. [CrossRef]
140. Liu, Z.; Lv, H.; Xie, Y.; Wang, J.; Fan, J.; Sun, B.; Jiang, L.; Zhang, Y.; Wang, R.; Shi, K. A 2D/2D/2D $Ti_3C_2T_x$@TiO_2@MoS_2 heterostructure as an ultrafast and high-sensitivity NO_2 gas sensor at room temperature. *J. Mater. Chem. A* **2022**, *10*, 11980–11989. [CrossRef]
141. Liu, P.; Feng, L.; Chen, H.; Li, P.; Ma, X.; Lv, M. Humidity sensor based on tapered no-core fiber coated with $Ti_3C_2T_x$ MXene. *Ceram. Int.* **2024**, *50*, 23586–23592. [CrossRef]
142. Waheed, W.; Anwer, S.; Khan, M.U.; Sajjad, M.; Alazzam, A. 2D $Ti_3C_2T_x$-MXene nanosheets and graphene oxide based highly sensitive humidity sensor for wearable and flexible electronics. *Chem. Eng. J.* **2024**, *480*, 147981. [CrossRef]
143. Yu, S.; Chen, C.; Li, P.; Zhang, H.; Zhang, H. Highly sensitive $Ti_3C_2T_x$ MXenes-RGO humidity sensor for human non-contact respiratory monitoring. *Sens. Actuators B* **2024**, *401*, 135014. [CrossRef]
144. Tang, K.; Ding, X.; Yu, X.; Lu, J.; Liu, F.; Li, H.; Chen, X. High fundamental frequency QCM humidity sensor based on C60-OH/$Ti_3C_2T_X$ nanocomposite with superior response. *Sens. Actuators B* **2025**, *426*, 137014. [CrossRef]
145. Han, Y.; Cao, H.; Cao, Y.; Wen, X.; Yao, Y.; Zhu, Z. Fast response flexible humidity sensors based on $Ti_3C_2T_x$ MXene-heterostructures for multifunctional applications. *J. Mater. Chem. C* **2024**, *12*, 4809–4816. [CrossRef]

Disclaimer/Publisher's Note: The statements, opinions and data contained in all publications are solely those of the individual author(s) and contributor(s) and not of MDPI and/or the editor(s). MDPI and/or the editor(s) disclaim responsibility for any injury to people or property resulting from any ideas, methods, instructions or products referred to in the content.